

INFORMATION TO USERS

This manuscript has been reproduced from the microfilm master. UMI films the text directly from the original or copy submitted. Thus, some thesis and dissertation copies are in typewriter face, while others may be from any type of computer printer.

The quality of this reproduction is dependent upon the quality of the copy submitted. Broken or indistinct print, colored or poor quality illustrations and photographs, print bleedthrough, substandard margins, and improper alignment can adversely affect reproduction.

In the unlikely event that the author did not send UMI a complete manuscript and there are missing pages, these will be noted. Also, if unauthorized copyright material had to be removed, a note will indicate the deletion.

Oversize materials (e.g., maps, drawings, charts) are reproduced by sectioning the original, beginning at the upper left-hand corner and continuing from left to right in equal sections with small overlaps. Each original is also photographed in one exposure and is included in reduced form at the back of the book.

Photographs included in the original manuscript have been reproduced xerographically in this copy. Higher quality 6" x 9" black and white photographic prints are available for any photographs or illustrations appearing in this copy for an additional charge. Contact UMI directly to order.

UMI

**A Bell & Howell Information Company
300 North Zeeb Road, Ann Arbor MI 48106-1346 USA
313/761-4700 800/521-0600**

**THE FLORIDA STATE UNIVERSITY
COLLEGE OF ARTS AND SCIENCES**

**INVERSE KINEMATICS PROTON SCATTERING WITH A
RADIOACTIVE ^{18}Ne BEAM**

**By
LEWIS A. RILEY**

**A Dissertation submitted to the
Department of Physics
in partial fulfillment of the
requirements for the degree of
Doctor of Philosophy**

**Degree Awarded:
Fall Semester, 1997**

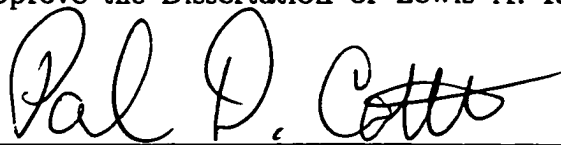
UMI Number: 9824610

UMI Microform 9824610
Copyright 1998, by UMI Company. All rights reserved.

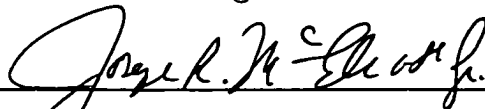
**This microform edition is protected against unauthorized
copying under Title 17, United States Code.**

UMI
300 North Zeeb Road
Ann Arbor, MI 48103

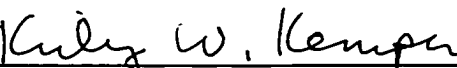
The members of the Committee approve the Dissertation of Lewis A. Riley defended on July 17, 1996.



Paul D. Cottle
Professor Directing Dissertation



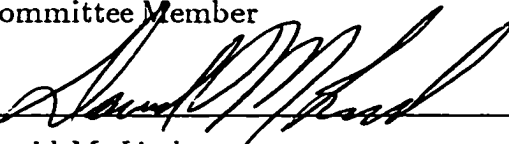
Joseph R. McElrath
Outside Committee Member



Kirby W. Kemper
Committee Member



Simon C. Capstick
Committee Member



David M. Lind
Committee Member

To Wendy

ACKNOWLEDGEMENTS

It is difficult to acknowledge all of the people who have contributed in different ways to this dissertation. I regret that I can only include some of them here.

First, I would like to thank Prof. Paul Cottle, for involving me in this work and serving as my advisor for the last four years. He provided guidance when I badly needed it and left me plenty of freedom to make the mistakes that have been essential to my education.

Thanks go to Dr. Thomas Glasmacher for setting an excellent example as a student and as a young nuclear physicist and for giving me the opportunity to work with him. The work could not have gone as smoothly without him. I would like to thank our other collaborators from FSU: Keith Jewell and Prof. Kirby Kemper; from the NSCL at MSU: Dr. Richard Ibbotson, Prof. David Morrissey, Heiko Scheit and Markus Chromik; and from IPN Orsay: Prof. Tiina Suomijärvi, Prof. Stephan Hirzebruch, Prof. Yurich Blumenfeld for their contributions to this project. I also wish to thank the technical staff at the NSCL for their help.

I am grateful to Dr. Vladimir Hnizdo for providing much needed assistance with our coupled channels calculations.

I would like to express my gratitude for the educational philosophy, adopted by the graduate programs in nuclear physics at both FSU and MSU, by which students are encouraged to get their hands dirty.

Although the experiment presented here was carried out far from home, many people at FSU have contributed to my education and thereby to this dissertation. Prof. Kirby Kemper has always given freely of his time, advice and broad knowledge of nuclear physics. I am grateful for his candor and insight. In addition, I would like to thank Dr. Simon Capstick, Prof. Mark Riley, Prof. Sam Tabor, Prof. Ray Sheline, Dr. Anthony Frawley, Dr. Edmund Myers and Dr. James Carr for their patience and insight in discussions which have helped me along the way. I am grateful to Dr. Mike Metlay for teaching me everything he knows about conversion electron spectroscopy. Powell Barber helped me to overcome countless technical

obstacles in my work. I also value his friendship, past and future. I would like to thank Dr. David Caussyn for his help with computer issues, Greg Brown, Gerry Hutchins and Phil Allen for their help with electronics and Dave Spingler and Van Griffin for their respective supervision of the LINAC and Tandem Accelerators. Special thanks go to Ray Willis, Kevin Kiley, Robin Chappell, Bobby Avant and Kenny Schaub in the nuclear research machine shop for teaching me my rudimentary machining skills, and for making the gadgets I couldn't manage on my own.

Lastly, I have to thank my office mates and other students, Keith Jewell, Jennifer Johnson, Bob Kaye, Geoff Sylvan, Tim Brown, Daryl Hartley, Glen Johns, Tim Drummer, Elizabeth Bartosz, Paul Cathers and Ed Reber, for their friendship, for sitting with the machine while I slept and for many lively discussions, some of them about physics.

CONTENTS

LIST OF TABLES	vii
LIST OF FIGURES	ix
ABSTRACT	xiii
1 Introduction	1
2 Overview of Theory	9
2.1 Structure of collective 2_1^+ states in light even-even nuclei	9
2.2 Sensitivities of experimental probes to protons and neutrons	16
2.3 Coupled channels calculations	21
3 Experimental Procedure	26
3.1 Inverse kinematics proton scattering	26
3.2 Experimental Details	30
3.2.1 Beam production	30
3.2.2 Beam tracking and identification	32
3.2.3 FSU-MSU particle telescope array	34
3.2.4 Electronics	39
4 Analysis and Results	44
4.1 Measurement of proton scattering angles	44
4.2 Proton angular distribution measurement	52
4.3 The lifetime of the 2_1^+ state of ^{18}Ne	57
4.4 Determination of M_n/M_p	58

5 Discussion	59
6 Summary	64
APPENDIX	65
BIBLIOGRAPHY	69
BIOGRAPHICAL SKETCH	75

LIST OF TABLES

2.1	Ratios of neutron to proton sensitivity of various probes [Ber81].	18
2.2	Optical potential parameters for ^{20}Ne [deS74].	24
A.1	Measured proton cross sections from the reaction $^1\text{H}(^{18}\text{Ne}, ^{18}\text{Ne}')\text{p}$ at 30 MeV/u taken from particle telescopes 1-3.	67
A.2	Measured proton cross sections from the reaction $^1\text{H}(^{18}\text{Ne}, ^{18}\text{Ne}')\text{p}$ at 30 MeV/u taken from particle telescopes 5-7.	68

LIST OF FIGURES

2.1	Qualitative sketches of the first few energy levels of vibrational and rotational nuclei.	13
2.2	Measured and calculated angular distributions of protons scattered from the ground state and 2_1^+ state of ^{20}Ne . The smooth curves are CC calculations using the optical potential parameters (see Table 2.2) and the RMS quadrupole deformation, $\beta_2 = 0.47$, deduced in [deS74]. For the solid curves, a vibrational model was used for the CC potential, and for the dashed curves, a rotational model was used. The measured cross sections of [deS74] are included for comparison.	25
3.1	Laboratory proton kinematics for the reaction $^1\text{H}(^{18}\text{Ne}, ^{18}\text{Ne}')\text{p}$ at 30 MeV/u. Lower energies in the laboratory correspond to forward scattering angles in the center of mass and to larger values of the differential cross section. The scattered beam particles are confined to a narrow forward cone of about 2.5° in scattering angle.	28
3.2	Schematic of the experimental arrangement.	29
3.3	Map of the experimental area of the National Superconducting Cyclotron Laboratory.	31
3.4	Schematic of the A1200 fragment separator	31
3.5	Position calibration spectrum for PPAC 1. An α source was used to irradiate a mask, with 2 mm diameter holes in a 1 cm square grid, placed over the active area. A quadratic calibration was used to produce linear position measurements over the central region spanned by the beam.	34

3.6	Sample beam identification spectra, the left column without and the right column with the shift in the photomultiplier bias voltage. (a) 0° detector fast vs. slow signals (b) Beam time of flight (TOF) vs. 0° detector slow signal.	35
3.7	Drawing of a single particle telescope from the FSU-MSU particle telescope array.	37
3.8	Diagram of the FSU-MSU particle telescope array. On the left, telescopes 1,2 and 3 are centered at 75° with respect to the beam axis, and telescope 4 is at 60.5° . On the right, telescopes 5,6 and 7 are centered at 70° , and telescope 8 is at 84.5°	38
3.9	Electronics diagram for a single particle telescope. Gates, and time starts were generated by the master electronics shown in Figure 3.11 and are not included explicitly here.	41
3.10	Electronics diagram for the beam detectors. Electronics for PPACs 1 and 2 were identical. Gates and time starts were generated by the master electronics shown in Figure 3.11 and are not included explicitly here.	42
3.11	Diagram of the master electronics which generated event triggers and gates. The boxed number in the coincidence logic units indicates the coincidence level required between the two inputs labeled A and B.	43

4.1	An arbitrary proton scattering event. The incoming beam particle with trajectory \vec{r}_{beam} is detected by the position sensitive PPACs at positions \vec{r}_1 and \vec{r}_2 and interacts with a proton in the target at position \vec{r}_{int} . The scattered proton is detected by a Si strip detector at an angle θ_0 , with respect to the optical axis, \hat{z} . The scattered proton trajectory, \vec{r}_p , is at an angle θ , the proton laboratory scattering angle, with respect to the incoming beam trajectory. For simplicity, the target is not shown at an angle with respect to the optical axis. .	45
4.2	Beam tracking spectra. Two dimensional position spectra for the beam measured at (a) PPAC 1 and (b) PPAC 2, and the projected (c) transverse position and (d) z position spectra on target.	47
4.3	Beam divergence spectrum. The FWHM is 0.9°	48
4.4	Illustration of the effects of target tilt on the spread in proton scattering angles, $\delta\theta$	49
4.5	Scattering angle correction spectra for (a) telescopes 1-3 and (b) telescopes 5-7.	50
4.6	(a) Proton laboratory kinetic energy vs. scattering angle plot. The dashed outline indicates inelastic scattering events to the 2_1^+ state. (b) Calculated kinematics for comparison. The solid box represents the total geometrical field of view of the telescopes, with the dashed lines showing the divisions between the telescope layers. The lower energy limit of the telescope field of view is due to the noise thresholds of the Si strip detectors. The upper limit is not physically meaningful.	53

4.7	Measured and calculated angular distributions of protons scattered from the ground state and 2_1^+ state of ^{18}Ne . The circular points correspond to data from telescopes 1-3, and the square points are from telescopes 5-7. The horizontal bars indicate the angular field of view of the strip(s), and the vertical bars give the statistical uncertainties. The smooth curves are CC calculations using ^{20}Ne optical model parameters taken from [deS74] and the RMS quadrupole deformation β_2 giving the best fit to the inelastic cross sections. The corresponding M_n/M_p value is included.	55
4.8	Summed proton laboratory kinematics spectra from (a) strips 4 of telescopes 1-3 and (b) strips 4 of telescopes 5-7.	56
5.1	The ratio M_n/M_p to N/Z for the 2_1^+ states of nuclei in the $12 \leq A \leq 26$ mass region from comparisons of electromagnetic (EM) [Ram87], proton scattering [DeL83, Gra80, Je:diss, deS74, Has83, Zwi83] and neutron scattering [Ols89, Gra80, Ols90] measurements. The open triangle is the reciprocal of the result for ^{18}O , the mirror partner of ^{18}Ne	60
5.2	The ratio M_n/M_p to N/Z for the 2_1^+ states of nuclei in the $12 \leq A \leq 26$ mass region. Pion scattering results [Pet93] are included along with the electromagnetic and nucleon scattering results of Figure 5.1. Dashed lines are calculations from [Bro82].	62

ABSTRACT

Angular distributions of protons scattered from the ground state and 1.89 MeV collective first $J^\pi = 2^+$ state of the $N = 8$ single closed shell nucleus ^{18}Ne , measured in inverse kinematics at 30 MeV/u at the National Superconducting Cyclotron Laboratory, are presented. This is the first inelastic proton scattering measurement of a proton-rich nucleus heavier than ^3He . The root-mean-square quadrupole deformation length of the first 2^+ state as measured via proton scattering, which is sensitive to a mixture of the neutron and proton deformation lengths, is extracted by comparison with a coupled channels calculation. When combined with the RMS deformation length of protons only, deduced from an existing γ ray lifetime measurement, this result yields a ratio of neutron to proton multipole matrix elements M_n/M_p for the first 2^+ state in ^{18}Ne of 0.38 ± 0.10 . This large departure from the collective model prediction of $M_n/M_p = N/Z = 0.8$ indicates that protons dominate the excitation, which is consistent with the shell model picture of relatively inert closed $N = 8$ and $Z = 8$ major shells. The systematic behavior of M_n/M_p for first 2^+ states in even-even nuclei in the $12 \leq A \leq 26$ mass region is discussed, and the dependence of M_n/M_p measurements on experimental probe is addressed.

CHAPTER 1

INTRODUCTION

Our understanding of the atomic nucleus has been shaped by two contrasting pictures. The first is of a collection of protons and neutrons filling a series of angular momentum states according to the Pauli principle, much like electrons in atomic systems. The second is of a nearly incompressible fluid drop subject to static and dynamic deformations and rotations. In fact, the distinction between the single particle and collective pictures is an artificial one. The Hamiltonian used in a single particle model is a collective mean field, and collective behavior can be understood in terms of the interactions of single particles. These two approaches can be viewed as defining the extrema on a continuum of nuclear behavior.

The already well developed atomic shell model provided a foundation for the development of a single particle nuclear model in the late 1940's. Observed isotopic abundances, nucleon separation energies, neutron capture cross sections and electric quadrupole moments all pointed to the existence of nuclear shell structure with "magic" numbers of protons and neutrons of 2, 8, 20, 28, 50, 82 and 126 [May48, Fee49, Nor49]. The spherical nuclear shell model, for which Maria Geoppert Mayer and J. Hans D. Jensen were awarded the Nobel Prize in 1963, was developed in light of these observations. The inclusion of a spin orbit coupling much stronger than that in atomic systems and which energetically favors states of higher total angular momentum turned out to be the key to producing the complete sequence of magic numbers, 2, 8, 20, 28, 50, 82 and 126, and correctly assigning many known ground state spins and parities [May49].

While the shell model was successful in describing nuclei near closed shells, it was less so in systems with many valence nucleons. Electric quadrupole moments are a measure of the deviation of the nuclear charge distribution from spherical shape. The systematic behavior of electric quadrupole moments had been one of the indicators of nuclear shell structure. However, away from closed shells, electric quadrupole moments were observed [Gor49, Tow49] which were much larger than the spherical shell model predicted and which came to be understood as arising from the polarization of closed shells by valence nucleons [Rai50]. The discovery of “core polarization” gave evidence for collective nuclear deformation and led to a renewed interest in a collective picture of the nucleus. A classical macroscopic treatment of the nucleus as a liquid drop with surface tension and compressibility had already been applied to the calculation of nuclear mass defects [Gam29] and also to the study of nuclear fission [Boh39], in which deviations from spherical shape are clearly important. In general, the shape of a liquid drop can be described by an expansion in the spherical harmonics,

$$R = R_0[1 + \sum \alpha_{lm} Y_{lm}(\theta, \phi)], \quad (1.1)$$

where R_0 is the mean radius, the α_{lm} are deformation amplitudes of multipole order l , and the Y_{lm} are spherical harmonics. The nuclear mean radius is generally given by $R_0 = r_0 A^{\frac{1}{3}}$, where $r_0 \approx 1.2$ fm. This formalism lent itself easily to the description of static nuclear deformations indicated by large electric quadrupole moments.

In 1941, Flügge explored the vibrational and rotational modes of excitation of the classical liquid drop [Flu41]. In this dynamical picture, the α_{lm} of Equation 1.1 are time dependent deformation amplitudes. The monopole term corresponds to a “breathing” mode and the dipole term to a translation of the center of mass. Since the nucleus is a relatively incompressible and heavy fluid these first two terms are not expected to be important in the low energy nuclear spectrum. Hence, it was expected that low-lying collective vibrations would be predominantly quadrupole in character.

The signatures of collective vibration are transition strengths many times the single particle prediction and a roughly harmonic energy level spacing where multiphonon excitations are observed. It eventually became apparent that low-lying quadrupole vibrations, having total angular momentum and parity $J^\pi = 2^+$, were present in the low energy spectra of many even-even nuclei away from closed shells [Sch55]. Evidence for octupole ($l = 3$) vibrations and for coupling between quadrupole and octupole modes followed, in the form of low lying negative parity 3^- and 1^- states, respectively [Ste54, Nat56, Ken56]. The classical liquid drop model was meanwhile more fully developed by Bohr and Mottelson into a quantized collective model of the nucleus for which they won a Nobel prize in 1975 [Boh52, Boh53, Boh75].

The first empirical evidence for nuclear collective motion did not come with the identification of a low energy surface vibration or rotational state, but rather as a more dramatic effect, the giant dipole resonance. Large broad resonances in (γ, n) and photo-fission reactions were observed in a wide range of nuclei for γ -ray energies on the order of 15-30 MeV [Bal47, Bal48]. These were successfully interpreted as a dipole vibration in which protons are driven by the oscillating electric field of the incident γ radiation, causing neutrons to vibrate opposite them [Gol48]. This mode can be handled in the formalism of Equation 1.1, if protons and neutrons are treated as two fluids with independent degrees of freedom [Ste50]. However, a schematic model describing the giant dipole resonances in terms of coherent combinations of single particle excitations was also successful [Bro61], an early indication that the collective and single particle pictures were not mutually exclusive.

The nature of the giant dipole resonance suggests that protons and neutrons may at times behave differently, even in collective motion. In 1932, shortly after the discovery of the neutron, Heisenberg proposed that the neutron and proton could be treated as two states of the nucleon [Hei32], yielding a new variable which came to be known as “isospin,” for isotopic- or isobaric- spin. A two component

isospin vector, mathematically identical to the Pauli spinors which describe spin, was added to the nucleon wavefunction. The new wavefunction could then be conveniently antisymmetrized according to the Pauli principle, and nuclear states, including collective states, could be assigned definite values of isospin. Nuclei exhibit approximate isospin symmetry. In other words, nuclear forces are nearly charge independent. Isospin symmetry is only approximate due to both the slight mass difference between the proton and neutron and small charge dependent components to nuclear interactions [Boh69]. The Coulomb interaction, due to proton charge, is the dominant effect breaking isospin symmetry, but it can be treated perturbatively.

In terms of isospin, nuclear states to which protons and neutrons contribute equally are termed “isoscalar,” and those for which proton and neutron contributions can be distinguished are termed “isovector.” The giant dipole resonance discussed above in which protons and neutrons vibrate against each other is an example of an isovector state. In the simplest collective picture, ignoring single particle effects such as shell structure, the collective quadrupole and higher order vibrational states discussed above are expected to be purely isoscalar in nature [Ber83]. However, the shell model predicts differences in proton and neutron vibrational amplitudes, principally due to shell closure. As with the giant resonances, low-lying collective vibrations are prime examples of nuclear behavior for which the interplay of the collective and single particle pictures is important.

It is possible, by comparison of transition strengths deduced from measurements using two properly chosen experimental probes, to separate the proton and neutron contributions to excited states. Experimental probes have been shown to have different sensitivities to protons and neutrons [Ber81]. With the exception of electromagnetic probes, such as electron scattering and Coulomb excitation, which are sensitive solely to protons, the available probes show mixed sensitivity. The most sensitive probes to neutrons are proton scattering at 10-50 MeV and π^+ scattering at

160-200 MeV, both of which interact approximately three times more strongly with neutrons in the target nuclei than protons. Conversely, neutron scattering at 10-50 MeV and π^- scattering at 160-200 MeV are three times as sensitive to protons.

The results of the comparisons of neutron and proton contributions to nuclear states can be conveniently expressed in terms of the ratio of their respective multipole transition matrix elements, M_n/M_p . The transition matrix element for protons (neutrons), $M_{p(n)}$, reduced with respect to angular momentum substates according to the Wigner-Eckart theorem, for a transition between the initial and final nuclear states $|\nu_i J_i T_i T_z A\rangle$ and $|\nu_f J_f T_f T_z A\rangle$ is given by

$$M_{p(n)} = \langle \nu_f J_f T_f T_z A || O_{\lambda}^{p(n)} || \nu_i J_i T_i T_z A \rangle \quad (1.2)$$

where $O_{\lambda,\mu}^{p(n)}$ is the multipole operator for a transition of order λ, μ for protons (neutrons), J is the total angular momentum, T is the isospin with substate $T_z = \frac{1}{2}(Z - N)$, A is the mass number, and ν represents any additional quantum numbers specifying the states. For a pure isoscalar state, M_n/M_p is simply the ratio of neutron to proton number, N/Z . For states with isovector contributions in which protons dominate we find $M_n/M_p < N/Z$, and when neutrons dominate, we find $M_n/M_p > N/Z$. In a simple shell model picture, closed shells are completely inert and thus should make no contribution to collective vibrations. If this were the case, we would expect M_n (M_p) to be zero for states in nuclei with closed neutron (proton) shells, giving $M_n/M_p = 0$ ($M_n/M_p = \infty$). In reality, closed shells are polarized by valence nucleons causing some overlap between core and valence nucleon wavefunctions in collective vibrations. Core polarization tends to moderate but not completely cancel the effects of shell closure [Ber83], and we see less dramatic departures in M_n/M_p from N/Z than predicted by the shell model with the assumption of inert closed shells. The approximate isospin symmetry of nuclear interactions leads

to the prediction [Ber79] for pairs of mirror nuclei that

$$M_{n(p)}(T_z) = M_{p(n)}(-T_z), \quad (1.3)$$

and hence that they should have approximately reciprocal M_n/M_p values.

The systematic behavior of M_n/M_p for 2^+ , and 3^- states in thirty-seven nuclei with $A \geq 40$ from proton scattering and electromagnetic data were compiled by Kennedy *et al.* using a consistent method of analysis in which similar isovector behavior is evident for the single closed proton shell isotopes, $^{116-124}\text{Sn}$ and the $N=82$ isotones, ^{138}Ba , ^{140}Ce and ^{144}Sm [Ken92]. In a similar consistent analysis of pion scattering data for even-even targets with $12 \leq A \leq 208$, Peterson compiled M_n/M_p values for 2^+ states in even-even nuclei in which the expected isovector behavior is observed in the presence of the $N = 8$ and $Z = 8$ closed shells in ^{14}C and ^{18}O and in the presence of the $N = 28$ and $Z = 28$ closed shells in ^{50}Ti , ^{52}Cr and $^{58,64}\text{Ni}$ [Pet93]. Isoscalar states in single closed shell nuclei are also observed in these data, indicating either the complete cancellation of shell closure effects by core polarization [Ber83] or the absence of the corresponding shell gap.

Until the 1980's, only stable or extremely long lived nuclei from which targets could be manufactured were accessible to electron, nucleon and pion scattering and Coulomb excitation experiments. Our understanding of differences in proton and neutron contributions to low-lying collective excitations was therefore limited to the roughly three hundred nuclei in and near the valley of stability. Since stable nuclei heavier than $A = 3$ have $N > Z$, due to the Coulomb repulsion between protons, we have also been limited mainly to the study of neutron-rich nuclei. The advent of radioactive beams has made it possible to perform both proton scattering in inverse kinematics [Kra94, Kel97] and Coulomb excitation [Ann95, Mot95, Sch96] with unstable nuclei. Hence, it is now possible to obtain M_n/M_p values for the nuclei away from stability, which were previously inaccessible and which comprise the lion's share of the approximately three thousand nuclei known to be particle

stable. Recent review articles [Mue93, Gei95] provide an overview of the current state of the art and future directions of research with radioactive beams.

The purpose of the present work is to expand the understanding of the systematic behavior of M_n/M_p for low-lying collective first excited $J^\pi = 2^+ (2_1^+)$ states in even-even nuclei at the $Z = 8$ proton and $N = 8$ neutron shell closures through an exploration of the unstable proton-rich single closed neutron shell nucleus, ^{18}Ne . M_n/M_p values indicating isovector behavior of 2_1^+ states in the stable nuclei ^{14}C ($N=8$) and ^{18}O ($Z=8$) have already been deduced [Pet93]. The mirror partners of these nuclei, ^{14}O ($Z=8$) and ^{18}Ne ($N=8$), respectively, are therefore of particular interest. However, of the two, only ^{18}Ne has a bound 2_1^+ state.

We present in this thesis the results of a proton scattering experiment in inverse kinematics using a radioactive ^{18}Ne beam at the National Superconducting Cyclotron Laboratory at Michigan State University. This is the first such measurement for a proton-rich nucleus heavier than $A = 3$. We extract an E2 transition strength from the measured proton angular distribution, yielding, in combination with an existing γ ray lifetime measurement [McD76], a value of M_n/M_p over a factor of two less than N/Z , indicating a large isovector component to the 1.89 MeV 2_1^+ collective quadrupole vibration in ^{18}Ne . This result is consistent with a picture of two valence protons, which dominate the vibration, outside relatively inert closed $N = 8$ neutron and $Z = 8$ proton shells. Our result for ^{18}Ne is qualitatively consistent with the behavior of the corresponding state in ^{18}O , in which the protons fill the $Z = 8$ shell and valence neutrons dominate. The observed isovector components to these states underscore the importance of shell effects in collective nuclear phenomena.

Chapter two of this thesis is an overview of the theory of collective excitations in light nuclei and of various means of studying the separate contributions of protons and neutrons to these excitations. Radioactive beam production and the details

of the inverse kinematics proton scattering measurement are discussed in chapter three. We present our analysis and results in chapter four, followed by a discussion of our findings in the context of the known systematics of the mass region in chapter five. In chapter six we provide a summary of our results and conclusions.

CHAPTER 2

OVERVIEW OF THEORY

In Section 2.1, we discuss the structure of the low-lying collective 2^+ states of interest in the present work. Section 2.2 is an overview of the various experimental probes which can be used to determine the proton and neutron contributions to excited states. The coupled channels calculations used to extract the root-mean-square quadrupole deformation length of the first 2^+ state of ^{18}Ne from our measured elastic and inelastic proton angular distributions is described in detail in Section 2.3.

2.1 Structure of collective 2_1^+ states in light even-even nuclei

In the framework of the shell model, nucleons in the ground state of an even-even nucleus fill the available nuclear orbitals of lowest energy, coupling in pairs of like nucleons to zero angular momentum. Each nucleon orbital angular momentum state, l , can couple to the nucleon spin to form two angular momentum states, $j = l \pm \frac{1}{2}$, each having $2j + 1$ substates, labeled $m = -j, -j + 1, \dots, j - 1, j$. According to the Pauli principle, these substates can be occupied by one nucleon of each type. The substates fill in pairs of time reversed orbitals m and $-m$, coupling to zero angular momentum. The parity of each substate is given by $(-)^l$. The total parity of each pair, which is the product of the parities of the individual nucleon wavefunctions, is therefore positive. Indeed, all known ground states of even-even nuclei have $J^\pi = 0^+$. Excited states are built by successive promotion of nucleons from the ground state configuration into unfilled nuclear shells and have angular momentum resulting from the coupling of the angular momenta of the excited nucleon(s) and the “hole(s)” left

in the ground state configuration. The parity of an excited state is given by the product of the parities of promoted nucleons. Excited shell model states with like spin and parity which are near to one another in excitation energy can interact with one another, and it is often the case that empirical results are best described by mixtures of various configurations.

Collective behavior can be treated in the shell model as a coherent mixture of many excited single particle configurations [Bro59]. Nuclear states are identified as collective by transition probabilities much larger than single particle predictions, indicating the participation of many nucleons. The transition probability per unit time for an electric (E) transition of multipole order λ is given by

$$T(E\lambda) = \alpha c \frac{8\pi(\lambda + 1)}{\lambda[(2\lambda + 1)!!]^2} \left(\frac{E_\gamma}{\hbar c}\right)^{2\lambda+1} B(E\lambda; i \rightarrow f) \quad (2.1)$$

where E_γ is the energy difference between the initial and final states. $B(E\lambda)$ is the reduced transition probability for an electric transition from an initial state $|\nu_f J_f M_f\rangle$ to a final state $|\nu_i J_i M_i\rangle$, given by

$$\begin{aligned} B(E\lambda; i \rightarrow f) &= \sum_{M_f \mu} |\langle \nu_f J_f M_f | O_{\lambda\mu}^E | \nu_i J_i M_i \rangle|^2 \\ &= \frac{1}{2J_i + 1} |\langle \nu_f J_f M_f || O_\lambda^E || \nu_i J_i M_i \rangle|^2, \end{aligned} \quad (2.2)$$

where $O_{\lambda\mu}^E$ is the electric multipole operator and the ν denote other quantum numbers specifying the states. The multipole operator for electric transitions is given by

$$O_{\lambda\mu}^E = \sum_p r_i^\lambda Y_{\lambda\mu}(\hat{r}_i), \quad (2.3)$$

where r_i is the radial position of the i^{th} proton. Note here that the proton transition matrix element, M_p , of Equation 1.2, for a transition of order λ is related to the reduced electric transition probability $B(E\lambda)$ above by

$$B(E\lambda; i \rightarrow f) = \frac{1}{2J_i + 1} M_p^2. \quad (2.4)$$

The commonly used single particle estimate [Bla79], known as the Weisskopf unit (W.u.), of an electric transition of multipole order λ is obtained, with the assumptions of a zero angular momentum final state and radial wavefunctions which are spheres of uniform density, giving,

$$\langle \nu_f J_f M_f | O_{\lambda\mu}^E | \nu_i J_i M_i \rangle = \sqrt{\frac{3}{4\pi R^3}} \int_0^R r^\lambda r^2 dr = \frac{1}{\sqrt{4\pi}} \frac{3}{3+\lambda} R^\lambda, \quad (2.5)$$

where $R = 1.2A^{1/3}$ fm is the nuclear radius. The Weisskopf single particle estimate is then given by,

$$B_W(E\lambda) = \frac{1}{4\pi} \left(\frac{3}{\lambda+3} \right)^2 1.2^{2\lambda} A^{2\lambda/3} f m^{2\lambda}. \quad (2.6)$$

We can make the qualitative statement that the integrals, $\langle \nu_f J_f M_f | O_{\lambda\mu}^E | \nu_i J_i M_i \rangle$, of Equation 2.2, involving the initial and final state wavefunctions contributing to the transition probability, will be larger for initial and/or final states which involve many nucleons behaving coherently than for the case where the states involve only single particles. Experimentally measured transition probabilities of tens to hundreds of W.u. are commonplace [Ald56]. The E2 transition, of interest in the present work, between the ground state and 1.89 MeV 2_1^+ state in ^{18}Ne has a reduced transition probability, from a γ ray lifetime measurement, of $B(E2; 0_{gs}^+ \rightarrow 2_1^+) = 17.7 \pm 1.7$ W.u. [McD76].

The collective model bypasses the microscopic treatment, and instead describes the macroscopic behavior of the system, as outlined in Chapter 1, giving a far more intuitive picture of collectivity than that yielded by the shell model. The two most widely observed types of collective motion, vibrations of the nuclear surface and rotations of deformed nuclear shapes, as well as mixtures of the two, appear in a systematic way across the chart of the nuclides. This systematic behavior maps onto the microscopic shell structure in a very clear way, supporting the idea that collective motion can be understood microscopically.

We focus here on collective 2_1^+ excitations, found in nearly all even-even nuclei. They are interpreted in the collective model as either quadrupole vibrations about a spherical or nearly spherical ground state equilibrium shape, or as rotations, with two units of angular momentum, of a permanently deformed ground state. Near closed shells, nuclei are nearly spherical in shape, and the dominant collective mode of excitation is vibrational, with an harmonic energy spacing, $\hbar\omega$, between successive phonon excitations. As valence nucleons are added, the ground states of the resultant nuclei are found to be further and further from spherical, as indicated by the observed large ground state quadrupole moments, reaching a maximum deformation at mid-shell. These permanently deformed nuclei exhibit very clear rotational behavior, characterized by an energy level spacing proportional to $J(J + 1)$. Qualitative sketches of the first few energy levels of vibrational and rotational nuclei are shown in Figure 2.1. The multiplets, in the vibrational case, corresponding to the various possible couplings of the angular momentum of successive vibrational phonons, are not expected to be truly degenerate or exactly harmonic, due to residual interactions between constituent configurations. The absence of rotational states with odd angular momentum in Figure 2.1 is a consequence of the invariance of the antisymmetrized wavefunctions under rotations [Boh75]. Rotational bands built on deformed intrinsic states with $J > 0$ have both odd and even angular momentum states.

Collective excitations in light ($A < 40$) nuclei consist of relatively few single particle configurations. However, the signature of collective behavior in the form of enhanced transition probabilities is observed, nonetheless. The level schemes of light nuclei are often truncated due to relatively weak binding, making it difficult to distinguish between vibrational and rotational behavior on the basis of level spacings. We have found that our coupled channels analysis, discussed in Section 2.3, of the proton scattering cross sections presented here, is not sensitive to the choice

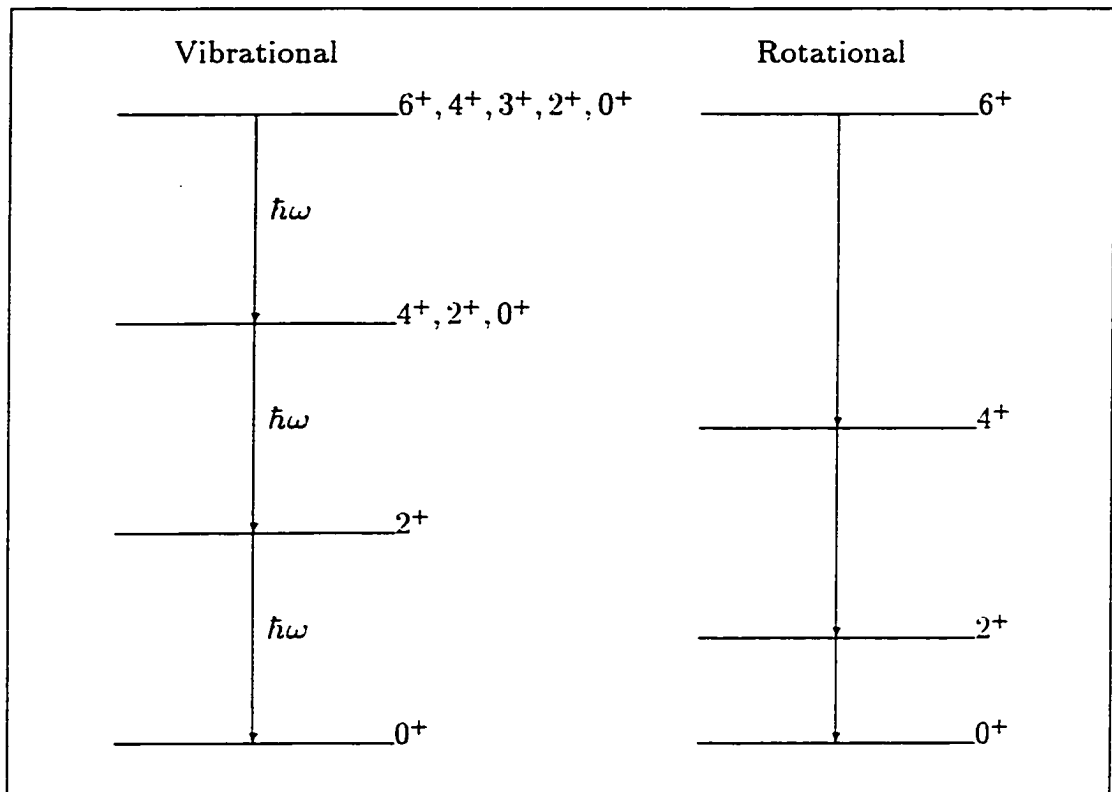


Figure 2.1: Qualitative sketches of the first few energy levels of vibrational and rotational nuclei.

of a vibrational or rotational model to describe the 2_1^+ state of ^{18}Ne . In the absence of evidence for one of these two pictures, our rather arbitrary choice of a vibrational model for our analysis carries no physical significance. In light nuclei, we speak of collectivity more in the sense of the coherent behavior of single particles, and less in the sense of the more easy to picture vibrations and rotations of a “liquid drop.”

The shell model, in addition to providing a map of the nature of collective excitations and deformations, gives us insight into the isospin composition of these states. Deviations from the simple collective model prediction of purely isoscalar collective states can usually be understood in terms of shell closure. It is a standard strategy within the shell model to treat filled major shells as inert and to describe

excited states solely in terms of valence nucleons [Boh69]. The closed shells form a spherical core, the influence of which is expressed, to first order, as an offset of the energy levels calculated in the valence space. In this simple scheme, a single closed shell (SCS) nucleus, having only valence protons (neutrons) has purely isovector excitations with a neutron (proton) transition matrix element (see Equation 1.2), $M_n = 0$ ($M_p = 0$). Along the same lines, collective behavior, consisting of many coherent single particle excitations, must be purely isovector in character as well. We expect, on the basis of this thinking, that isovector behavior will be maximal in a given mass region, in SCS nuclei.

In a more realistic shell model approach, attempts are made to take into account mixing between excited valence nucleons and excitations of nucleons in the core [Bro75, Bro80, Bro82]. This approach is certainly plausible given that, at least in light nuclei, the spherical core is itself a known, stable nucleus with bound excited states (^4He , ^{16}O , ^{40}Ca and ^{48}Ca). This coupling to the core is termed “core polarization,” and is quantified in terms of polarization parameters which connect the proton and neutron transition matrix elements, A_n and A_p , calculated in the shell model valence space to the corresponding full matrix elements, M_n and M_p , as follows,

$$\begin{aligned} M_p &= A_p(1 + \epsilon_{pp}) + A_n\epsilon_{pn} \\ M_n &= A_n(1 + \epsilon_{nn}) + A_p\epsilon_{np} \end{aligned} \quad (2.7)$$

where the ϵ_{ab} give the coupling of the valence nucleons b to the core nucleons a . In this formalism, a SCS nucleus, for which A_p (A_n) is zero, is not limited to purely isovector excitations, since the core protons (neutrons) can contribute, with non-zero ϵ_{pn} (ϵ_{np}), to M_n (M_p). Hence, core polarization acts to moderate the extreme isovector behavior predicted using the valence shell model configurations.

Bernstein *et al.* [Ber81] use a schematic model [Bro75] to set the polarization parameters of Equation 2.7 based on coupling to the isoscalar and isovector giant resonances in the core, and show good agreement with measured M_n/M_p ratios for $0^+ \rightarrow 2^+$ transitions in both proton and neutron valence SCS nuclei over the mass range $18 \leq A \leq 208$. Madsen and Brown [Mad84] have extended this model to treat open shell nuclei between $N = 50$ and $N = 82$, in which a rapid return to isoscalar behavior is observed, moving away from closed shells.

Some results of shell model calculations including core polarization by Brown *et al.* [Bro82] for 2_1^+ states in sd nuclei ($8 \leq N, Z \leq 20$) are discussed in relation to the present work in Chapter 5. Core polarization is included as outlined above. The shell model calculations are performed using an ^{16}O inert core, with $n = A - 16$ valence nucleons treated in a complete $0d_{5/2}, 1s_{1/2}, 0d_{3/2}$ basis, denoted by the shorthand $(sd)^n$. Under the assumption of one body interactions, the model space transition matrix elements $A_{p(n)}$ are separated into one body transition densities, $D_{\lambda,p(n)}^{n,i,f,T_z}$, and single particle matrix elements (SPME) of the multipole transition operator $O_{p(n)}^\lambda$ (see Equation 2.3) as follows,

$$\begin{aligned} A_{p(n)}(T_z) &= \langle (sd)^n \nu_f J_f T_f T_z || O_{p(n)}^\lambda || (sd)^n \nu_i J_i T_i T_z \rangle \quad (2.8) \\ &= \sum_{jj'}^{sd} \text{SPME}[O_{p(n)}^\lambda(jj')] D_{\lambda,p(n)}^{n,i,f,T_z}(jj'), \end{aligned}$$

where j and j' are the angular momenta of the particle and hole involved in a single particle transition and the nuclear wavefunctions $|(sd)^n \nu J T T_z\rangle$ are written in terms of the sd shell model basis according to a diagonalization of the particle and hole Hamiltonian of Chung and Wildenthal [Bro80b]. The densities, D_λ , containing all of the information about the single particle composition of the total wavefunctions, are given by,

$$D_{\lambda,p(n)}^{n,i,f,T_z} = \frac{1}{\sqrt{2\lambda + 1}} \langle (sd)^n \nu_f J_f T_f T_z || (a_j^\dagger \otimes \bar{a}_{j'})_{p(n)}^\lambda || (sd)^n \nu_i J_i T_i T_z \rangle, \quad (2.9)$$

where a_j^\dagger and $\bar{a}_{j'}$ are the creation operators for a nucleon in orbit j and a nucleon hole in orbit j' , which are coupled here to a resultant angular momentum λ . The SPME are written,

$$\text{SPME}[O_{p(n)}^\lambda] = \langle \rho_j || O_{p(n)}^\lambda || \rho_{j'} \rangle, \quad (2.10)$$

where the ρ_j are single particle wavefunctions. The calculations of [Bro82] presented in Chapter 5 were performed using single particle wavefunctions from a phenomenological local Woods Saxon nuclear potential. They adopt core polarization parameters, $\epsilon_{pp} = \epsilon_{nn} \approx 0.15$ and $\epsilon_{pn} = \epsilon_{np} \approx 0.55$, based on a fit to measured proton and neutron transition matrix elements in the mass region. In the cases of ^{18}O and ^{18}Ne , an expanded $0p_{1/2}, 0d_{5/2}, 1s_{1/2}$ basis of Zucher, Buck and McGrory [Zuc68] was used in calculating the D_λ in order to account for excitations in ^{16}O not included in the treatment of core polarization.

2.2 Sensitivities of experimental probes to protons and neutrons

The proton and neutron multipole transition matrix elements, M_n and M_p of Equation 1.2, are independent of the experimental probe(s) used to measure them. With the exception of electromagnetic (EM) probes, which only interact with protons and thus measure M_p directly, various experimental probes interact with both protons and neutrons, measuring mixtures of M_n and M_p [Ber81]. The multipole transition operator $O_{\lambda\mu}^F$ for an experimental probe F is therefore a mixture of the corresponding neutron and proton operators, $O_{\lambda\mu}^{Fn}$ and $O_{\lambda\mu}^{Fp}$,

$$O_{\lambda\mu}^F = b_n^F O_{\lambda\mu}^{Fn} + b_p^F O_{\lambda\mu}^{Fp}, \quad (2.11)$$

where the $O_{\lambda\mu}^{Fp(n)}$ are related to, but have a different radial dependence from, the multipole operators $O_{\lambda\mu}^{p(n)}$ of Equation 2.3 [Ost79]. The multipole matrix element measured by a probe F is then given by,

$$M_F = \langle \nu_f J_f T_f T_Z A || O_\lambda^F || \nu_i J_i T_i T_Z A \rangle$$

$$= b_n^F M_n + b_p^F M_p, \quad (2.12)$$

where b_n^F and b_p^F are the neutron and proton external field strengths for the probe F , which can be thought of as measures of the sensitivity of the probe to neutrons and protons, respectively. Thus, M_n and M_p can be extracted from measurements of M_F and M_G with two experimental probes F and G having different sensitivities to protons and neutrons.

In practice, the transition matrix element of a transition of multipole order λ , for a given hadron scattering probe, is obtained in the form of the root-mean-square (RMS) multipole deformation length $\delta_\lambda^F = r_0^F \beta_\lambda^F$, which is extracted from the measured elastic and inelastic differential cross sections with a coupled channels or folding model analysis. The mean radius, r_0^F is probe dependent, and the β_λ^F are unitless RMS deformation parameters, corresponding to the $\alpha_{\lambda 0}$ of the multipole expansion of the nuclear radius in Equation 1.1. The measured RMS deformation length is again a mixture of the proton and neutron deformations,

$$\delta_\lambda^F = \frac{b_n^F N \delta_\lambda^n + b_p^F Z \delta_\lambda^p}{b_n^F N + b_p^F Z}. \quad (2.13)$$

With the relation,

$$\frac{M_n}{M_p} = \frac{N \delta_\lambda^n}{Z \delta_\lambda^p}, \quad (2.14)$$

and Equation 2.13 we obtain M_n/M_p in terms of the RMS deformation lengths measured by two probes, F and G , of different proton and neutron sensitivity,

$$\frac{M_n}{M_p} = \frac{\epsilon_G^F \frac{\delta_\lambda^F}{\delta_\lambda^G} - 1}{\frac{b_n^F}{b_p^F} - \frac{b_n^G}{b_p^G} \epsilon_G^F \frac{\delta_\lambda^F}{\delta_\lambda^G}} \quad (2.15)$$

where we have defined,

$$\epsilon_G^F = \frac{1 + \frac{N b_p^F}{Z b_n^F}}{1 + \frac{N b_n^G}{Z b_p^G}}. \quad (2.16)$$

The approximate ratios b_n^F/b_p^F , listed in Table 2.1, for various experimental probes in specific energy ranges are compiled by Bernstein, Brown and Madsen in

Table 2.1: Ratios of neutron to proton sensitivity of various probes [Ber81].

Probe (F)	Energy [MeV]	b_n^F/b_p^F
EM	–	0
(p, p')	10 - 50	≈ 3
(n, n')	10 - 50	$\approx \frac{1}{3}$
$(\pi^+, \pi^{+'})$	160 - 200	≈ 3
$(\pi^-, \pi^{-'})$	160 - 200	$\approx \frac{1}{3}$
(p, p')	800	0.83
(p, p')	1000	0.95
(α, α')	All	1

Reference [Ber81], in which the approximations are shown to be consistent among the various probes to within about 15% over a wide mass range ($18 \leq A \leq 208$). We present a comparison of low energy nucleon scattering and 160-200 MeV pion scattering measurements in the $12 \leq A \leq 26$ mass region in Chapter 5. We therefore discuss here the proton and neutron sensitivities of these probes in detail.

The ratio b_n^N/b_p^N for inelastic scattering of nucleons (N) from nuclei in the energy range 10-50 MeV is based on the phenomenological optical potentials for nucleon elastic scattering. The optical potential V_N for elastic scattering of nucleons from a nucleus with proton and neutron numbers Z and N can be written in terms of its isoscalar and isovector components as follows [Sat83],

$$V_N = V_0 + V_1 \frac{4}{A} \vec{\tau} \cdot \vec{T} \quad (2.17)$$

where $\vec{\tau}$ and \vec{T} are the isospin operators of the incident nucleon and target nucleus, and V_0 and V_1 contain the respective isoscalar and isovector potential form factors

and well depths. For protons ($\tau_z = \frac{1}{2}$) and neutrons ($\tau_z = -\frac{1}{2}$), we obtain

$$V_N = V_0 \pm V_1 \frac{(N - Z)}{A} \begin{cases} n \\ p \end{cases} \quad (2.18)$$

Ground states of self conjugate ($N = Z$) target nuclei have isospin projection $T_z = 0$, and the isovector term vanishes, leaving a purely isoscalar potential.

In the following discussion, we assume that isoscalar and isovector components of the optical potential of Equation 2.18 have identical form factors, and further that the ratios of imaginary to real parts of V_0 and V_1 are identical. Based on the current understanding of effective NN interactions, the ratio of the isoscalar to isovector potentials, V_0/V_1 , is found to lie between -2 and -3 for low energy nucleon scattering, the latter being the Serber limit, in which odd relative angular momentum interactions are ignored, and the former resulting from more realistic potentials [Car85]. Bernstein *et al.* take the value -2 [Ber81, Mad75], for which the ratio of the optical potentials seen by protons and neutrons is

$$\begin{aligned} \frac{V_p}{V_n} &\approx \frac{V_0 \left[1 + \frac{(N-Z)}{2A} \right]}{V_0 \left[1 - \frac{(N-Z)}{2A} \right]} \\ &\approx \frac{3N + Z}{N + 3Z}, \end{aligned} \quad (2.19)$$

where the coefficients of N and Z in the numerator and denominator are the respective probe sensitivities for protons and neutrons. Hence, $b_n^p = b_p^n \approx 3$ and $b_p^p = b_n^n \approx 1$, giving the sensitivity ratios of Table 2.1. If we take the Serber limit, $V_0/V_1 = -3$, we obtain $b_n^p = b_p^n \approx 2$ and $b_p^p = b_n^n \approx 1$.

In the energy range 160-200 MeV, the lowest lying pion nucleon (πN) Δ resonance, with $l = 1, T = J = \frac{3}{2}$ (generally denoted P_{33}), dominates the $N(\pi^\pm, \pi^\pm)N$ scattering cross section. Scattering of pions from nuclei in this energy range can be treated in the impulse approximation, in which we think of the incident pions as interacting with individual nucleons rather than with some bulk nuclear potential.

Multiple πN scattering and NN interactions complicate this picture. [Eis80] However, the πN interactions are characterized by the angular momentum and isospin of the P_{33} resonance, and the favored isospin coupling determines the relative sensitivities of π^\pm to protons and neutrons.

Pions are isospin $\tau_\pi = 1$ particles, having three charge states π^+, π^0 and π^- , and nucleons have isospin $\tau_N = \frac{1}{2}$. We use the conventions that the nucleon isospin substate $\tau_{Nz} = +\frac{1}{2}$ is the proton, and the pion substates $\tau_{\pi z}$ correspond to pion charge. Expanding the coupled $\pi^\pm p$ systems in terms of states of good isospin $\vec{T} = \vec{\tau}_\pi + \vec{\tau}_N$, denoted $|T, T_z\rangle$, we have

$$\begin{aligned} |\pi^+ p\rangle &= \left| \frac{3}{2}, \frac{3}{2} \right\rangle \\ |\pi^- p\rangle &= \sqrt{\frac{1}{3}} \left| \frac{3}{2}, -\frac{1}{2} \right\rangle - \sqrt{\frac{2}{3}} \left| \frac{1}{2}, -\frac{1}{2} \right\rangle, \end{aligned} \quad (2.20)$$

and similarly for $\pi^\mp n$,

$$\begin{aligned} |\pi^- n\rangle &= \left| \frac{3}{2}, -\frac{3}{2} \right\rangle \\ |\pi^+ n\rangle &= \sqrt{\frac{1}{3}} \left| \frac{3}{2}, \frac{1}{2} \right\rangle + \sqrt{\frac{2}{3}} \left| \frac{1}{2}, \frac{1}{2} \right\rangle, \end{aligned} \quad (2.21)$$

where the $|T, T_z\rangle$ are orthonormal. On the P_{33} resonance, only the amplitudes (Clebsch-Gordan coefficients) associated with the resonant $\left| \frac{3}{2}, T_z \right\rangle$ components of the coupled $\pi^\pm N$ states of Equations 2.20 and 2.21 contribute to the scattering amplitudes. The $T = \frac{3}{2}$ projection operator is given by

$$\Pi_{\frac{3}{2}} = \sum_{T_z} \left| \frac{3}{2}, T_z \right\rangle \left\langle \frac{3}{2}, T_z \right| \quad (2.22)$$

We obtain the approximate ratios of probe sensitivity, $b_n^{\pi^\pm}/b_p^{\pi^\pm}$ at the P_{33} resonance from ratios of the expectation values of $\Pi_{\frac{3}{2}}$ as follows

$$\frac{b_p^{\pi^\pm}}{b_n^{\pi^\pm}} \approx \frac{\langle \pi^\pm n | \Pi_{\frac{3}{2}} | \pi^\pm n \rangle}{\langle \pi^\pm p | \Pi_{\frac{3}{2}} | \pi^\pm p \rangle} = \begin{cases} \frac{1}{3} & (\pi^+) \\ 3 & (\pi^-) \end{cases}, \quad (2.23)$$

where the result is approximate, since there is a small non-resonant background under the P_{33} resonance.

2.3 Coupled channels calculations

Coupled channels (CC) calculations were performed in the present work using the computer code CHUCK [Kunz]. In particular, the CC calculations were used to extract the dynamic deformation parameter β_2 of the 2_1^+ state in ^{18}Ne from our elastic and inelastic proton angular distributions measured in the proton scattering experiment. CHUCK performs a numerical integration of a system of coupled equations, of the form [Comf]

$$\left[\frac{d^2}{dr_c^2} - \frac{l_c(l_c + 1)}{r_c^2} + (k_c^2 - U_{cc}) \right] \chi_{j_c l_c}^J(k_c; r_c) = \sum_{c' \neq c} \frac{2\gamma_c}{\hbar^2} V_{cc'} \chi_{j_{c'} l_{c'}}^J(k_{c'}; r_{c'}), \quad (2.24)$$

where the channel wavefunctions, $\chi_{j_c l_c}^J(k_c; r_c)$, describe the relative motion of the projectile and target in the channel c , with the relative coordinates \vec{r}_c and wavenumber k_c , and γ_c is the reduced mass of the system. The channel wavefunctions are the constituents of a partial wave expansion in l_c , the orbital angular momentum of the projectile about the target. The total angular momentum J is given by $\vec{J} = \vec{l}_c + \vec{s}_c + \vec{I}_c$, where s_c and I_c are the respective intrinsic angular momenta of the projectile and target. The angular momentum coupling scheme, $\vec{j}_c = \vec{l}_c + \vec{s}_c$, is used, for which the $\vec{l}_c \cdot \vec{s}_c$ interaction is diagonal. The diagonal potential, U_{cc} , contains an optical potential, generally based on optical model analyses of observed elastic cross sections. The off-diagonal coupling term, $V_{cc'}$, describes transitions, and hence the effective interaction, between channels c and c' . In CHUCK, both U_{cc} and $V_{cc'}$ include the Coulomb interaction, and the nuclear potentials are determined by the user. Elastic and inelastic scattering with various combinations of projectile and target excitations and orientations, as well as one or two nucleon transfer reactions, in the zero-range approximation, can be included as channels.

There are n independent solutions to the n coupled Equations 2.24 where n is the number of channels included. The physical solution, generally a linear combination of the solutions calculated, is selected with the application of boundary conditions in the far field and at the origin [Comf]. The nuclear potentials in U_{cc} and $V_{cc'}$ are short range, leaving only the Coulomb interaction in the far field, yielding the condition that the solution must be a linear combination of the Coulomb functions at large r_c . In addition, wavefunctions are required to go to zero at the origin. The scattering amplitudes for the exit channels, from which the differential cross sections are calculated, are contained in the corresponding physical solutions.

In choosing the optical potential U_{cc} for the analysis of inverse kinematics proton scattering from ^{18}Ne , presented in Section 4.2, we followed the calculations of de Swiniarski *et al.* [deS74] for ^{20}Ne , using a real Wood Saxon (WS) volume potential and an imaginary WS surface absorption, along with a spin orbit term with a volume WS form factor. The volume WS form factor is given by

$$f(x_i) = \frac{1}{[1 + e^{x_i}]}; \quad x_i = \frac{r_c - r_i A^{\frac{1}{3}}}{a_i} \quad (2.25)$$

where the subscript i refers to the real (R), imaginary (I) or spin orbit (SO) potential, A is the target mass number, and the V_i , r_i and a_i are the potential well depth, radius and diffuseness parameters, respectively. The surface WS form factor is the first derivative of the volume form factor with respect to x_i . The optical potentials used have the explicit form,

$$U_{cc} = \frac{2\gamma}{\hbar^2} \left[-V_R f(x_R) + iV_I \frac{df(x_I)}{dx_I} + V_{Coulomb}^{Elastic}(r_c) + V_{SO} \frac{1}{r_c} \frac{df(x_{SO})}{dr_c} \vec{l}_c \cdot \vec{s}_c \right]. \quad (2.26)$$

In a simple vibrational model, the coupling potentials, $V_{cc'}$, are the first order term in an expansion of each potential in U_{cc} about its equilibrium radius. Neglecting the

spin orbit potential and assuming a pure quadrupole vibration,

$$V_{cc'} = \beta_2 \left[V_R r_R \frac{df(x'_R)}{dx'_R} - i V_I r_I \frac{d^2 f(x'_I)}{dx'^2_I} + r_{c'} V_{Coulomb}^{Inelastic}(r_{c'}) \right] \times \sum_m D_m^2(\epsilon_t) Y_{2m}(\hat{r}_{c'}), \quad (2.27)$$

where β_2 is the RMS quadrupole deformation of the target in the inelastic channel, the $D_m^2(\epsilon)$ perform a rotation through the Euler angles ϵ of the Y_{2m} , the spherical harmonics of order 2, and ϵ_t represents the Euler angles connecting the channel coordinates to the intrinsic reference frame of the target nucleus. The signs of potentials in Equations 2.26 and 2.27 are such that attractive potentials have positive well depth parameters, V_i .

In the present work, we include in Equations 2.24 only the channels for which we observed appreciable cross sections, namely those corresponding to proton scattering from the ground state and 2_1^+ state of ^{18}Ne . For simplicity, protons were treated as projectiles and ^{18}Ne nuclei as targets in the calculations. In all entrance channels, the ^{18}Ne nucleus is in its ground state, with angular momentum and parity $I_c^\pi = 0^+$. Hence, only the relative orbital angular momentum and the proton spin contribute to J , and $J^\pi = j_c^{(-)^{l_c}}$. In the exit channels, $l_{c'} = 0$ for elastic scattering, $l_{c'} = 2$ for scattering to the 2_1^+ state, and $\vec{J} = \vec{j}_{c'} + \vec{l}_{c'}$ with the constraint that $l_c + l_{c'}$ must be even to conserve parity. For each entrance channel with $l_c \geq 2$, there are six exit channels, one elastic and five inelastic channels, which conserve J^π , yielding a set of six coupled equations. For $l_c < 2$, J is not conserved for scattering to the 2_1^+ state, leaving only the elastic exit channel.

As a test of our method, we reproduced the results of de Swiniarski *et al.* [deS74] for ^{20}Ne , using the optical potential parameters listed in Table 2.2. The results of this test, along with the measured cross sections from [deS74], are shown in Figure 2.2. We obtain very similar results from our CC calculations, performed using a vibrational model, to the those of de Swiniarski, *et al.* which were performed

Table 2.2: Optical potential parameters for ^{20}Ne [deS74].

V_R	r_R	a_R	V_I	r_I	a_I	V_{SO}	r_{SO}	a_{SO}
[MeV]	[fm]	[fm]	[MeV]	[fm]	[fm]	[MeV]	[fm]	[fm]
44.3	1.10	0.73	27.84	1.38	0.60	31.20	1.03	0.74

using a rotational model with the computer code ECIS. We include a rotational model CHUCK calculation as the dashed curves in Figure 2.2, which do not differ appreciably from the solid vibrational model curves. Grabmayr *et al.* report a similar insensitivity of their CC calculations, performed using CHUCK, to the choice of a vibrational or rotational model in their analysis of inelastic nucleon scattering data for the 2_1^+ state in ^{18}O [Gra80].

Calculated cross sections for elastic scattering and inelastic scattering to the 2_1^+ state of ^{18}Ne are presented in the analysis of the measured proton angular distributions of the present work in Section 4.2. In all CC calculations presented here, integrations were performed to 10 fm with a 0.1 fm step size, and 20 partial waves were included.

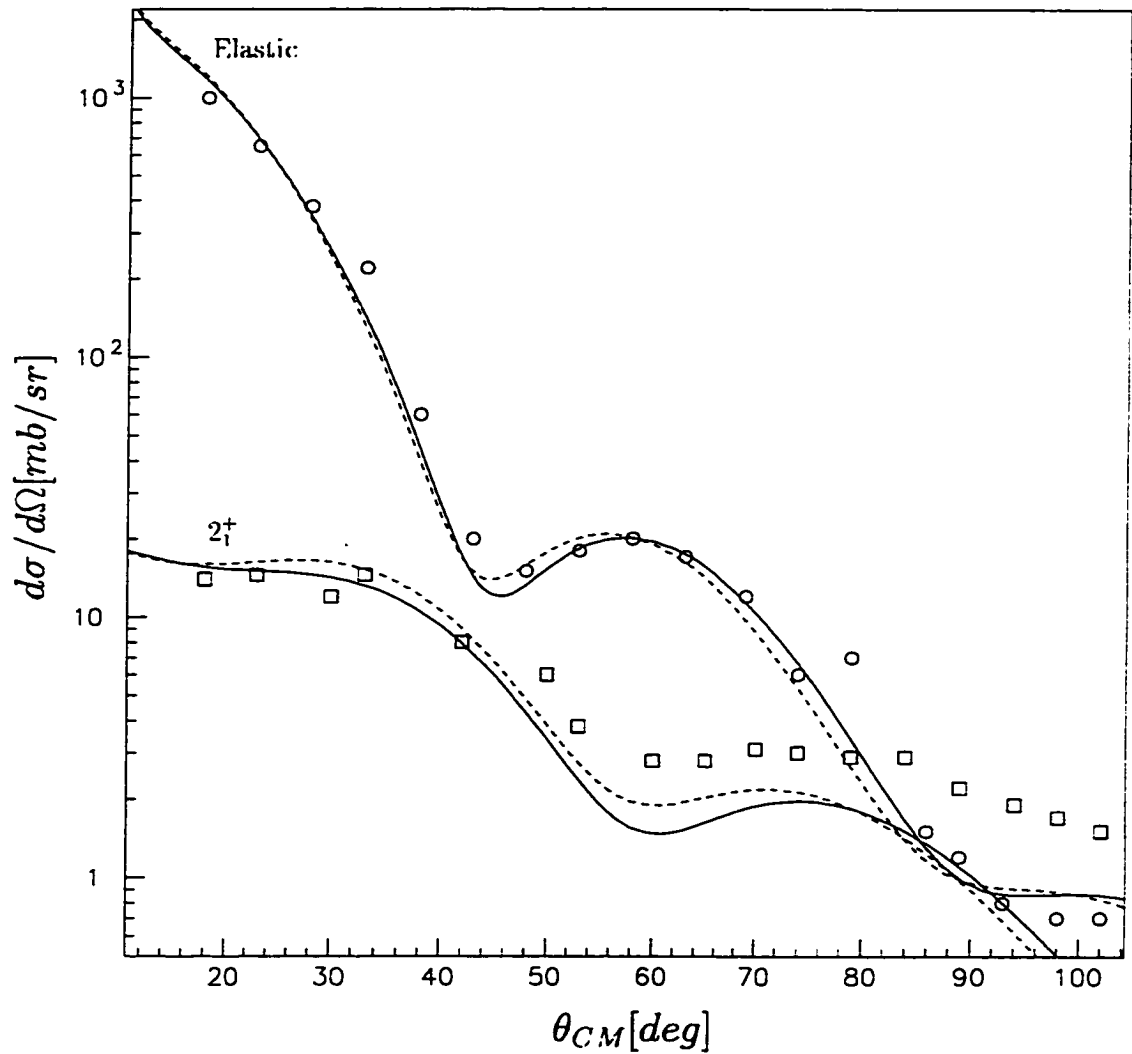


Figure 2.2: Measured and calculated angular distributions of protons scattered from the ground state and 2_1^+ state of ^{20}Ne . The smooth curves are CC calculations using the optical potential parameters (see Table 2.2) and the RMS quadrupole deformation, $\beta_2 = 0.47$, deduced in [deS74]. For the solid curves, a vibrational model was used for the CC potential, and for the dashed curves, a rotational model was used. The measured cross sections of [deS74] are included for comparison.

CHAPTER 3

EXPERIMENTAL PROCEDURE

3.1 Inverse kinematics proton scattering

Inelastic proton scattering differs from Coulomb excitation in that the nuclear force, rather than the electromagnetic force, dominates the interaction between projectile and target. This gives rise to the difference in neutron and proton sensitivities of these probes discussed in Section 2.2. Proton scattering at low energies ($T_p \leq 50$ MeV) is not a spectroscopically complete probe, meaning that it excites certain nuclear states preferentially, favoring low-lying single particle and single phonon collective modes.

Forward kinematics proton scattering, in which a proton beam is incident on a stationary target, is limited to the study of roughly three hundred nuclei in the valley of stability from which targets can be made. However, with the advent of radioactive beams, inverting the kinematics of the reaction has become a feasible way to collect equivalent data for thousands of unstable isotopes. The exchange of projectile for target in inelastic proton scattering changes the kinematics of the reaction in the laboratory but has no effect on the nuclear interactions we wish to study. The main limitation of this technique over standard proton scattering is that radioactive beams generally have low intensities. Radioactive beams produced by primary fragmentation at the NSCL (see Section 3.2.1) range in luminosity from 10^7 particles/second (pps) for nuclei close to stability down to a few pps out near the drip lines [She91].

Secondary beams produced by primary fragmentation typically have large angular divergence and large transverse profiles on target, both of which can have

unacceptable effects on the resolution of angular measurements. Collimation is an effective method of controlling these problems but involves a significant loss of beam intensity. An upper limit is placed on beam intensity of about 10^5 pps by the read-out times of beam identification detectors. Hence, if beam intensities on this order can be reached with collimation, beam tracking is unnecessary. If collimation introduces an unacceptable loss of beam, tracking on an event by event basis is an attractive alternative. We chose beam tracking for the present work, in which the maximum beam intensity produced was 3×10^4 pps, and we present a comparison of our method with an estimate of the effects of beam collimation in Section 4.1.

The laboratory frame proton kinematics for elastic scattering and inelastic scattering from the 2_1^+ state of ^{18}Ne , in the reaction $^1\text{H}(^{18}\text{Ne}, ^{18}\text{Ne}')\text{p}$ at 30 MeV/u, appear in Figure 3.1 in the form of a kinetic energy vs. proton scattering angle plot. An interesting feature of the kinematics is that protons are scattered into large angles in a rather narrow range in the laboratory, from about 65° - 85° . Lower energies in the laboratory correspond to forward scattering angles in the center of mass and also thus to larger values of the differential cross section. The scattered beam particles are confined to a narrow forward cone of about 2.5° in scattering angle, allowing easy detection of scattered beam particles with a single detector at 0° .

Some form of stationary proton target is required for proton scattering in inverse kinematics. Provided reaction products of the beam on ^{12}C do not present insurmountable problems, solid plastic targets are an attractive option. In the case of ^{18}Ne at 30 MeV/u, products of the beam on carbon are directed forward of the angular range of elastically and inelastically scattered protons. We used $(-\text{CH}_2-\text{CH}=\text{CH}-)_n$ (polypropylene) targets, making a measurement with a ^{12}C target as a check for any resulting background. High purity cryogenic hydrogen targets are a more technically difficult option.

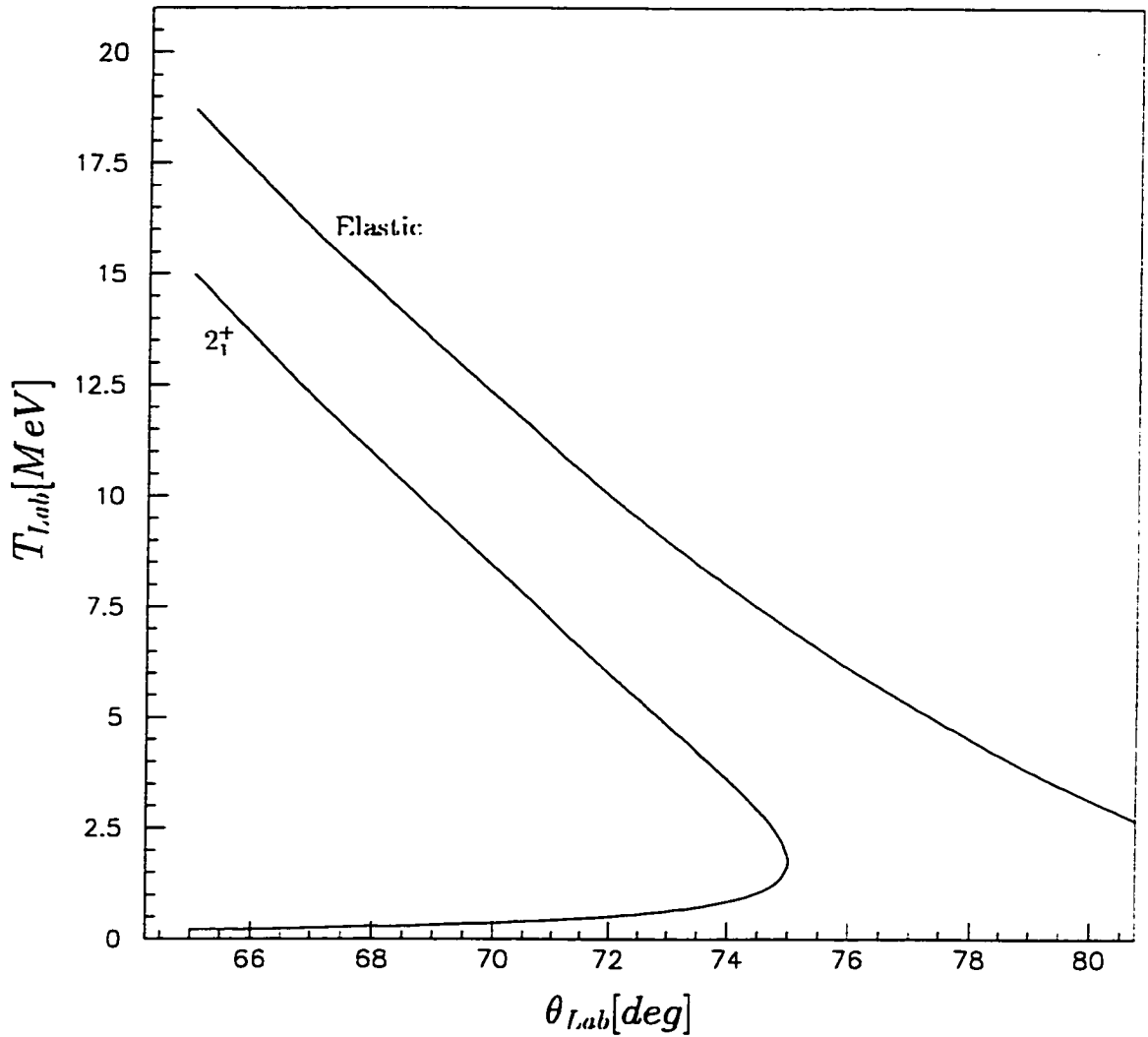


Figure 3.1: Laboratory proton kinematics for the reaction ${}^1\text{H}({}^{18}\text{Ne}, {}^{18}\text{Ne}')\text{p}$ at 30 MeV/u. Lower energies in the laboratory correspond to forward scattering angles in the center of mass and to larger values of the differential cross section. The scattered beam particles are confined to a narrow forward cone of about 2.5° in scattering angle.

A schematic of the experimental arrangement can be found in Figure 3.2. We tracked the beam on an event by event basis with two position sensitive parallel plate avalanche counters (PPACs) [Swa94] and stopped the beam in a fast/slow plastic phoswich detector (0° detector) used for isotope selection. We detected scattered

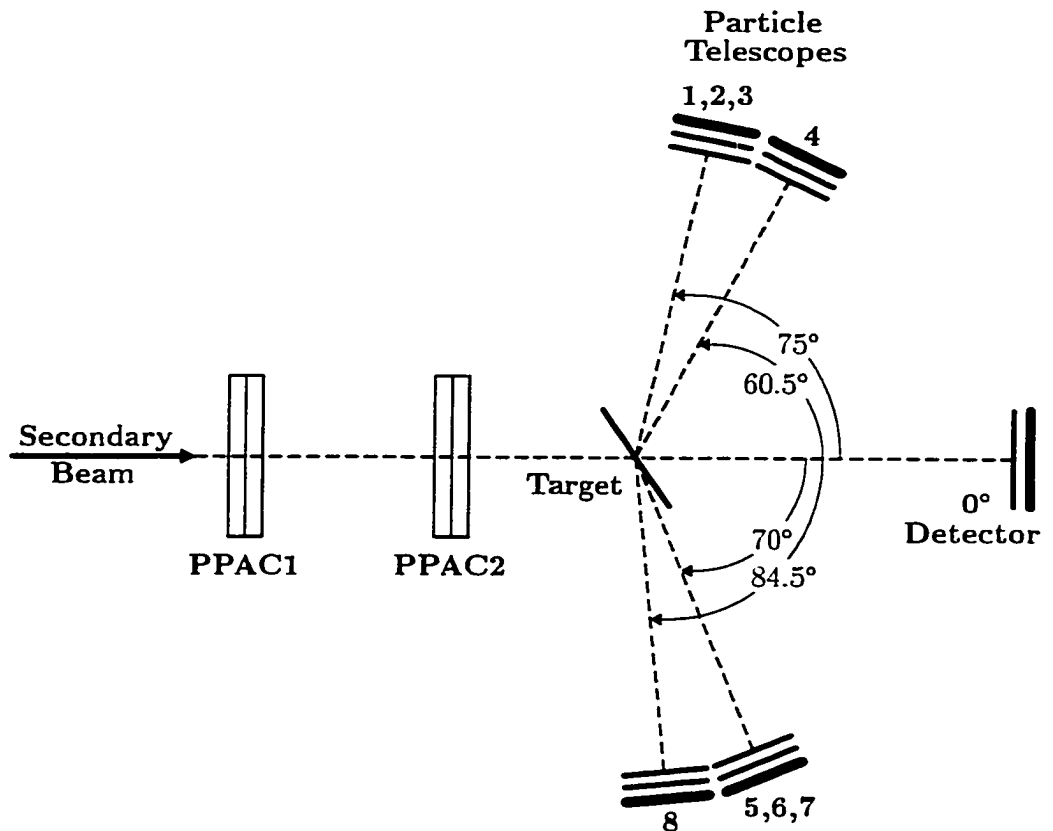


Figure 3.2: Schematic of the experimental arrangement.

protons using the FSU-MSU array of eight Si Strip-Si PIN-CsI particle telescopes, mounted in the MSU 92" scattering chamber, installed in the S2 vault, which houses the Superball neutron detector, at the exit of the RPMS fragment separator (see Figure 3.3). The detection system is described in greater detail in Section 3.2. We collected a total of 10,764 clean proton events in an energy range of 1-22 MeV and scattering angle range of 65° - 82° . This translates to a forward kinematics angular range of roughly 20° - 45° in the center of mass, corresponding to the region of the first maxima in the elastic and inelastic differential cross sections.

3.2 Experimental Details

3.2.1 Beam production

Radioactive beams are produced at the NSCL by means of projectile fragmentation. A primary beam, produced in an electron cyclotron resonance ion source (ECR), accelerated by the K1200 superconducting cyclotron to a few tens to hundreds of MeV/u and incident on a water cooled primary target, produces a wide array of forwardly directed fragments at close to the primary beam energy. The isotopes of choice are then selected in the A1200 projectile fragment separator [She91], yielding a secondary beam which requires no acceleration. Figure 3.3 is a map of the of the experimental areas of the NSCL. The A1200 is located between the K1200 and the transfer hall, allowing radioactive beams to be delivered to all target areas. Radioactive fragments traverse a total path length through the A1200 and transfer beam lines on the order of a few tens of meters before reaching the secondary target, with traverse times on the order of hundreds of ns. Only fragments with lifetimes longer than the traverse time are accessible by this method.

Figure 3.4 is a schematic of the layout of the A1200. The A1200 has two stages, each built around two superconducting dipole magnets which turn the beam in opposite directions. The system of quadrupole doublets and triplets are included to make the device achromatic, and the sextupoles correct for aberrations. Each stage can be tuned to a different magnetic rigidity, $B\rho$, where B is the dipole magnetic field strength and ρ is the radius of curvature of the beam path, which selects the beam charge to mass ratio by the relation $B\rho = p/q$, where p is the beam momentum, and q is its charge state. Secondary beams, fully stripped of electrons, are then selected by each stage of the A1200 by their atomic mass to charge ratio A/Z . The acceptance of the A1200 is controlled by momentum slits, which limit the range of transmitted beam momentum and therefore the range of beam rigidity.

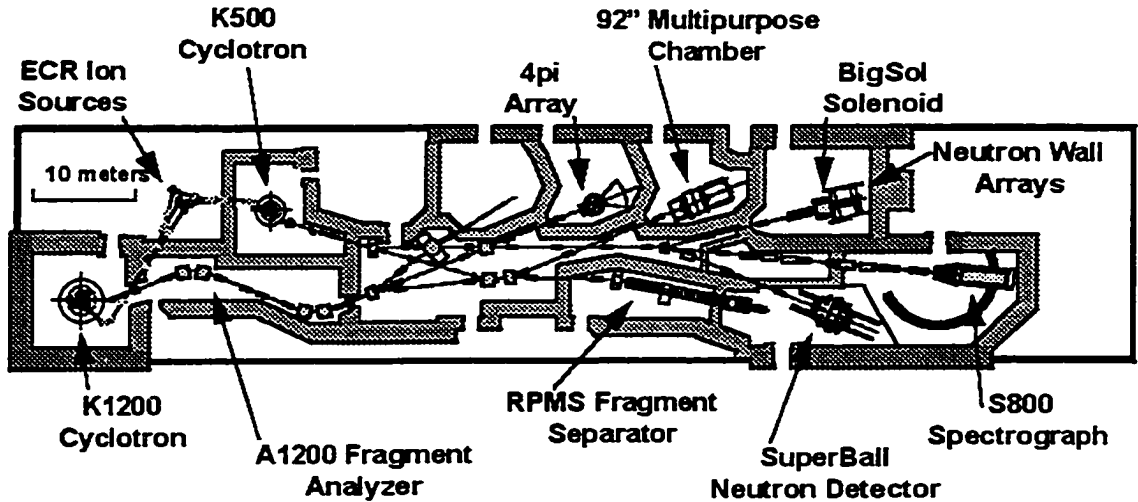


Figure 3.3: Map of the experimental area of the National Superconducting Cyclotron Laboratory.

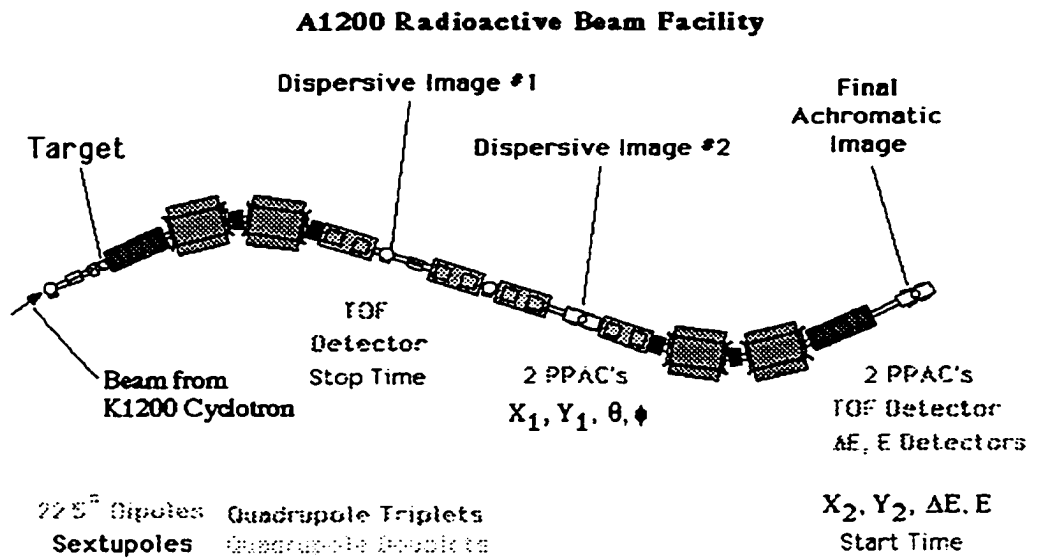


Figure 3.4: Schematic of the A1200 fragment separator

A single stage of the A1200 is sufficient for separation by A/Z . Separation by charge number, Z , is then possible with time of flight and energy measurements. The advantage of a two stage system is that it allows the inclusion of intermediate

dispersive images, where the beam is distributed spatially by momentum. Thin degrading materials can then be placed at these dispersive images in order to further separate isotopes in the beam and therefore to reduce the number of isotopes transmitted by the second stage of the A1200. The energy loss of ions in a thin degrader is proportional, in the non relativistic limit, to dA^3/Z^2 , where d is the thickness of the material [Ann87]. The overall rigidity of the beam is reduced, and the velocity spread between beam species of different atomic mass is increased. The second stage of the separator must therefore be tuned to a lower rigidity, and a smaller range of mass numbers is transmitted. Achromatic degrading wedges are tapered to preserve the achromatic nature of the A1200, and are used when the full momentum acceptance of the system is needed.

We used a primary beam of ^{20}Ne at 65 MeV/u, a ^9Be primary target (360 mg/cm²) and a ^{12}C degrading wedge (200 mg/cm², 1.9 mrad) at the second dispersive image position to produce a secondary beam of ^{18}Ne at 30 MeV/u. The traverse time of the beam from the primary to the secondary target was 910 ns, which is well within the 1672 ms half life of ^{18}Ne . With a primary beam intensity of about 50 particle nA (pnA), we obtained up to 30,000 pps on target. The beam was approximately 90% pure. ^{17}F was the main contaminant at about 7%.

3.2.2 Beam tracking and identification

The beam was tracked by two position sensitive parallel plate avalanche counters (PPAC) [Swa94], placed at 1 m and 2 m upstream of the target. The PPACs are position sensitive in two dimensions over a 10×10 cm² active area. A total of about 0.4 mg/cm² of aluminized polyester and polypropylene in the electrodes and low pressure iso-octane gas introduce homogeneous energy losses and negligible angular straggling to the beam. Simple charge division readouts, two for the x and two for the y positions, require minimal electronics. Fast preamplifiers are used, capable of handling counting rates up to 5×10^4 events/second.

From the raw PPAC signals, designated left, right, up and down (L, R, U, and D), raw positions were calculated as follows,

$$x_{raw} = \frac{L - R}{L + R} \quad (3.1)$$

$$y_{raw} = \frac{U - D}{U + D} \quad (3.2)$$

We made position calibration measurements for each PPAC, using an α source to irradiate a mask placed over the active area. The mask had a square grid of 2 mm diameter holes with 1 cm spacing, a fine grid in the center with 1 mm spacing and an L shaped pattern to insure proper orientation. Quadratic calibrations were sufficient to correct the nonlinear raw positions in the central region spanned by the beam. The position calibration spectrum for PPAC 1 is shown in Figure 3.5. A position resolution of 2 mm was observed. The positions of the centers of the PPACS with respect to the beamline axis were measured using an alignment telescope and were added to the offsets of the PPAC calibrations. However, these additional offsets are not included in Figure 3.5.

The beam was stopped in a fast/slow plastic phoswich telescope mounted at 0° (the 0° detector) with an acceptance of 2.5° in scattering angle. The beam time of flight (TOF) was also measured, using a PIN diode located at the exit of the A1200 and the 0° detector as the start and stop detectors, respectively. The fast and slow signals of the 0° detector provide a $\Delta E - E$ measurement, allowing isotope separation by mass and charge number. The counting rate limitation of the 0° detector is on the same order as that of the PPACS. A sporadic shifting of the photomultiplier bias voltage during the experiment led to difficulties in the separation of the ^{17}F contaminant from the ^{18}Ne . However, we were able to achieve unambiguous beam identification with a beam time of flight vs. 0° slow signal measurement. Sample beam identification spectra, with and without the bias voltage shift are included in Figure 3.6.

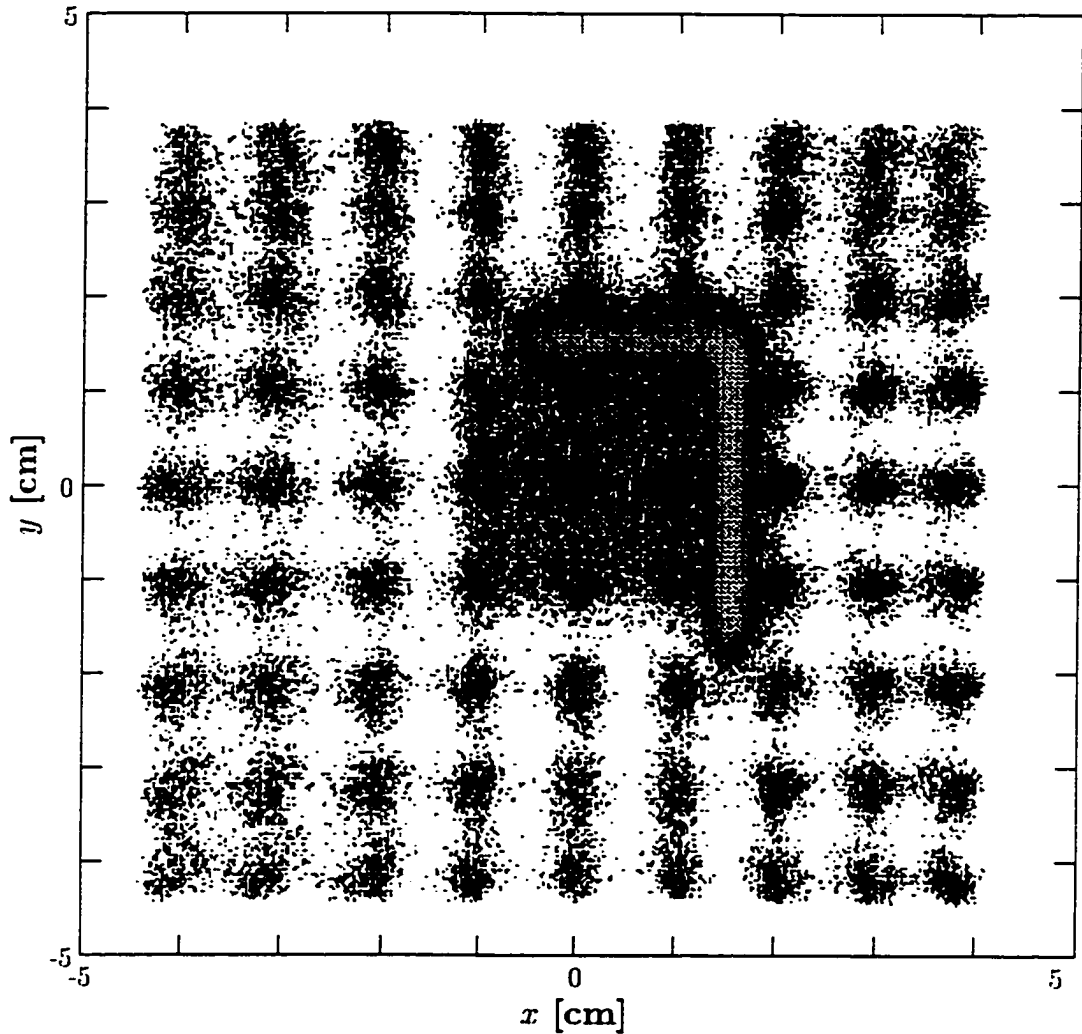


Figure 3.5: Position calibration spectrum for PPAC 1. An α source was used to irradiate a mask, with 2 mm diameter holes in a 1 cm square grid, placed over the active area. A quadratic calibration was used to produce linear position measurements over the central region spanned by the beam.

3.2.3 FSU-MSU particle telescope array

Scattered protons were detected using the FSU-MSU array of 8 Si strip-Si PIN-CsI particle telescopes. A detailed drawing of a single telescope is shown in Figure 3.7. Each stage of the telescopes has an active area of $5 \times 5 \text{ cm}^2$. The $\approx 300 \mu\text{m}$ thick strip detectors consist of 16 strips, 3 mm wide, which are read out in distinct

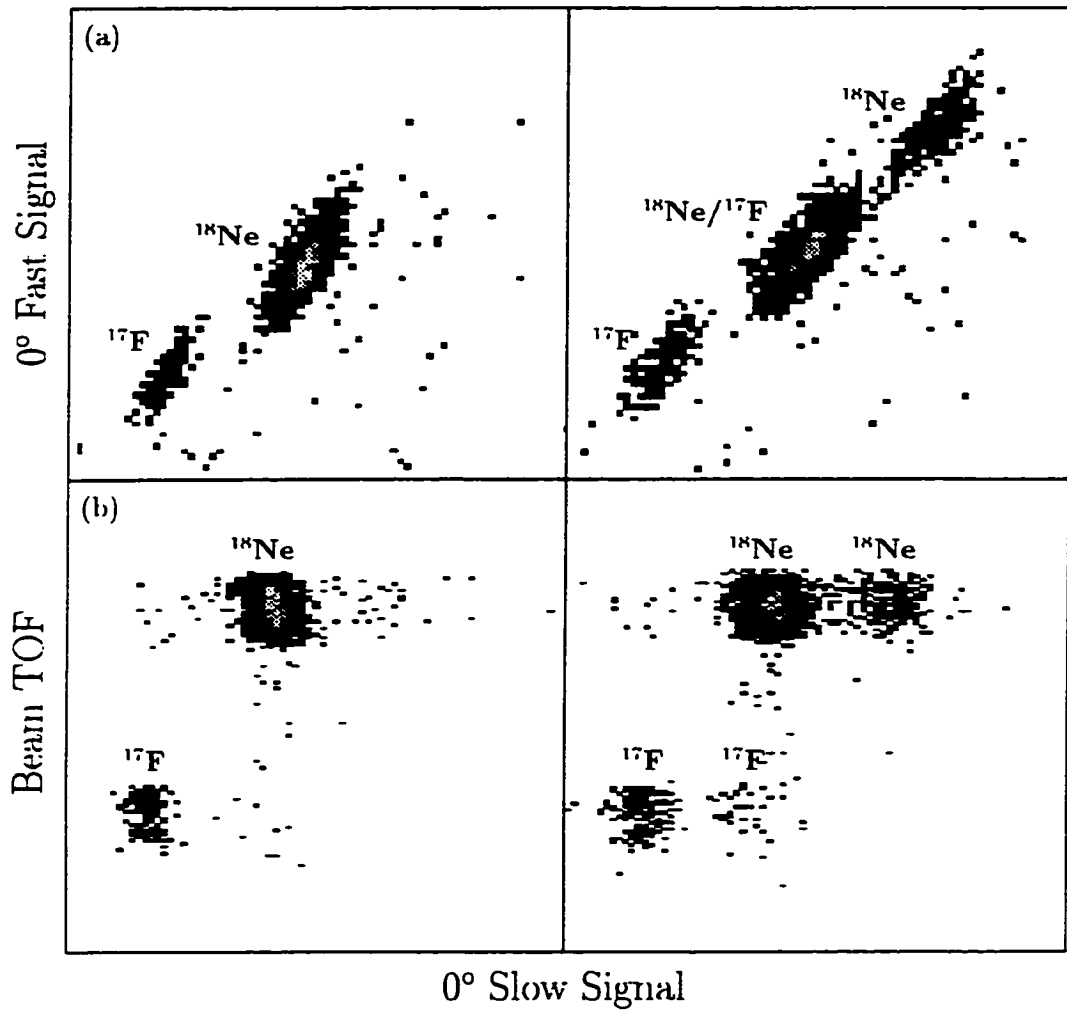


Figure 3.6: Sample beam identification spectra, the left column without and the right column with the shift in the photomultiplier bias voltage. (a) 0° detector fast vs. slow signals (b) Beam time of flight (TOF) vs. 0° detector slow signal.

channels. The $\approx 470 \mu\text{m}$ PIN diode and 1 cm CsI layers stopped higher energy particles. Each Si PIN diode consists of a doped n -type Si wafer with a rectifying junction to a very thin p -type layer on one surface. Electrical contacts are made to evaporated gold layers on the front and back surfaces of the wafer. The rectifying junctions and electrical contacts amount to less material than the equivalent of a

0.1 μm Si layer [Kno79]. The detector, when operated under reverse bias, is fully depleted, allowing for charge collection over nearly its entire thickness. The Si strip detectors are segmented PIN diodes, each strip having its own isolated electrical contacts, giving a discrete position sensitivity in one direction. Light from each CsI detector was collected by four Si photodiodes coupled to the crystal with clear RTV epoxy.

Particles stopped in the strip detectors were identified by time of flight, while higher energy particles could be identified in $\Delta E - E$ mode. Energy calibration spectra were measured with all Si strip and Si PIN detectors using a ^{228}Th α source. These were used to correct for differences between detectors. We then obtained an energy calibration for protons for each particle telescope as a whole by fitting the on-line proton elastic scattering data to the calculated kinematic curve (see Figure 3.1). We detected protons in the energy range 1-22 MeV. Protons with energies below ≈ 6.8 MeV were stopped in the Si strips. Those with energies between ≈ 6.8 MeV and ≈ 11.5 MeV stopped in the Si PINs, and higher energy protons were stopped by the CsI layers.

Preamplifiers used with the particle telescope array were built at MSU. The preamplifiers for the Si PIN diodes and the photodiodes used with the CsI detectors were placed inside the vacuum chamber. Shielded cables and feedthroughs were used to deliver signals to the external electronics. Due to space constraints, it was not practical to mount the preamplifiers for the Si strip detectors inside the target chamber. Longer cables between the strip detectors and preamplifiers and somewhat poorer shielding from the environment led to nearly quadruple the noise observed in the Si PIN diodes. The Si PIN diode noise thresholds corresponded to roughly 230 keV, while the Si strip thresholds were close to 1 MeV.

The telescopes as mounted for the present work are shown in Figure 3.8 (see also Figure 3.2). Each telescope was mounted to one of two vertical support beams on

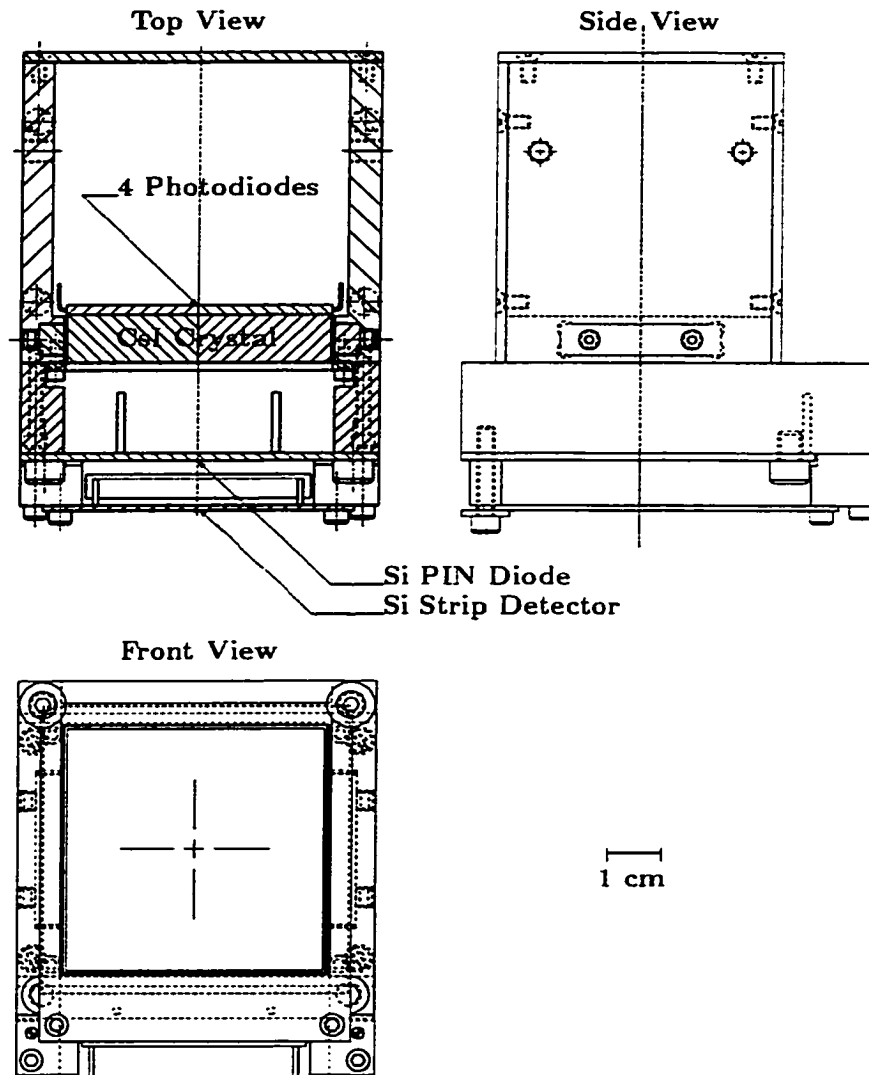


Figure 3.7: Drawing of a single particle telescope from the FSU-MSU particle telescope array.

a beveled wedge designed such that the Si strips were tangent to circles of constant scattering angle with respect to a coordinate system with origin at the target center and z-axis collinear with the beamline axis. The telescopes were mounted 28 cm from the target position, yielding a total geometric field of view of 10° for each telescope and 0.6° for each strip. Due to a large beam profile on target and to the fact that the strips were not curved to follow lines of constant scattering angle,

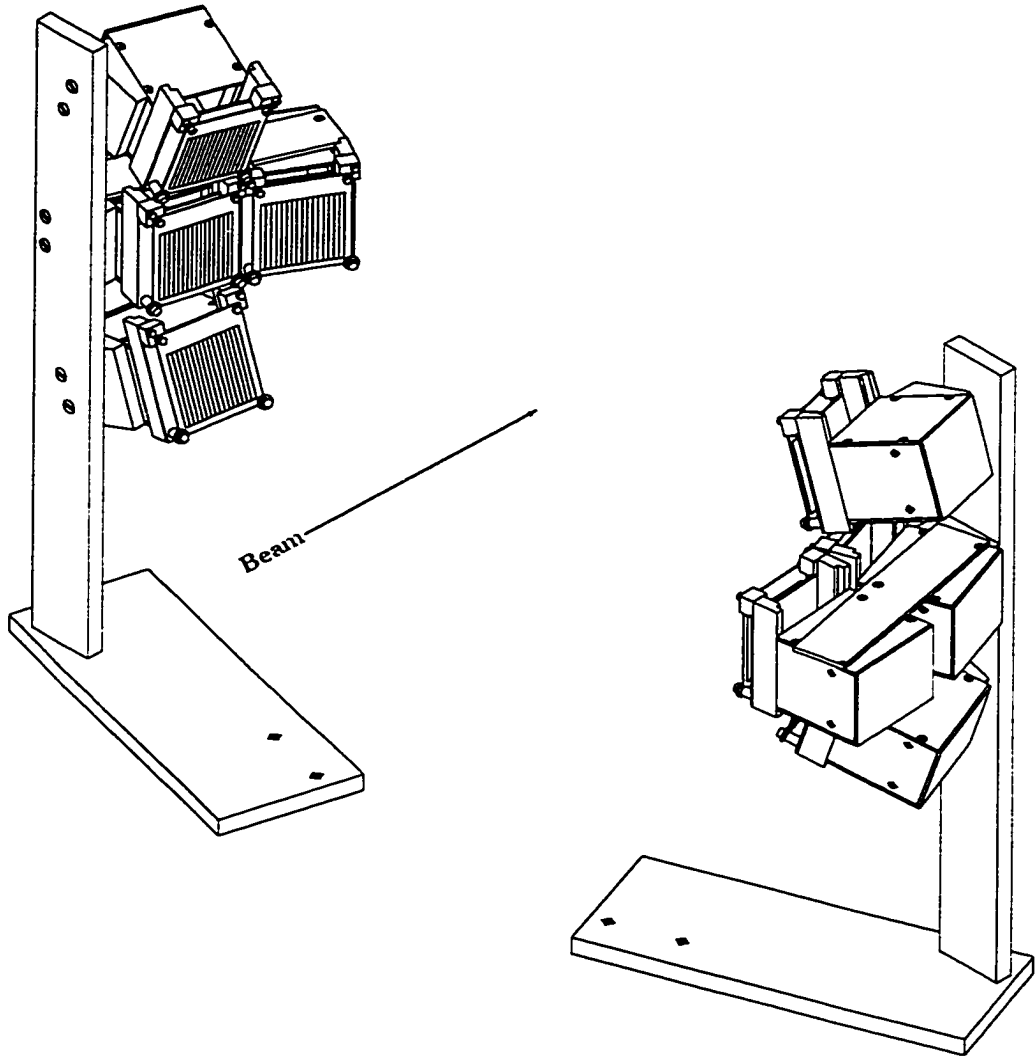


Figure 3.8: Diagram of the FSU-MSU particle telescope array. On the left, telescopes 1,2 and 3 are centered at 75° with respect to the beam axis, and telescope 4 is at 60.5° . On the right, telescopes 5,6 and 7 are centered at 70° , and telescope 8 is at 84.5° .

the effective angular acceptance of each strip, corresponding to an uncertainty in angular measurements, was approximately 0.85° .

Three telescopes (designated 1, 2 and 3) were mounted with their centers at a scattering angle of 75° and three (designated 5, 6 and 7) were centered at 70° . Telescopes 4 and 8 were centered at 60.5° and 84.5° to increase the overall angular

coverage, but due to threshold and electronics problems, they did not yield reliable data. The large divergence of the secondary beam widened the overall angular field of view of the array. This effect is discussed in Section 4.1. We detected protons in a laboratory scattering angle range of $65^\circ - 82^\circ$, or a forward kinematics proton scattering angle range of roughly $20^\circ - 45^\circ$ in the center of mass, corresponding to the region of the first maxima in the differential cross sections for elastic scattering and scattering from the 2_1^+ state in ^{18}Ne .

3.2.4 Electronics

A diagram of the electronics associated with a single particle telescope is shown in Figure 3.9. Si strip energies were digitized in 16 channel analog to digital converters (ADC). Si strip time signals were generated by fast time to charge converters (TFC), started by the acquisition system trigger, stopped by signals from the strip constant fraction discriminators (CFD), and read out by fast encoding and readout ADCs (FERA). The strip CFD signals were also fed to 16 channel scaler modules. In similar fashion, energy and time signals were generated for the Si PIN diodes, the only difference being that times were read out using standard time to digital converters (TDC). Separate energy and scaler signals were produced for each of the four photodiodes used to detect the light from each CsI crystal. The logic OR output of a Si strip detector CFD module indicated a signal above the noise threshold in any one of its 16 channels. The Si strip CFD OR outputs from all 8 particle telescopes were fed into a discriminator/latch with a logic SUM output, which generated a signal for any event above noise threshold in any Si strip of any telescope.

Electronics for the beam timing, tracking and identification detectors are diagrammed in Figure 3.10. Charge is collected in four channels from each PPAC corresponding to left, right, up and down. PPAC timing signals are produced by fast amplifiers mounted with the PPACs in the beamline. The 0° fast and slow signals were read out by FERAs. The 0° detector preamplifier also produced a fast

timing pulse. This timing pulse was used, along with the logic SUM signal of all of the Si strip detectors, by the master logic circuit, described below, to trigger data acquisition. The 0° fast and slow signals were read out by FERAs.

We used the standard NSCL data acquisition hardware and software. [Fox89] Two types of online events were acquired, scattered protons in coincidence with recoiling beam particles, and downscaled beam events. A master logic circuit, shown in Figure 3.11, was used to trigger the acquisition system. A coincidence logic unit (CLU) labeled "Master" in Figure 3.11 required both an event in any Si strip detector and a 0° detector event. Hence, a "Master" coincidence signified a possible proton event. Downscaled beam events were triggered by a logic pulse from a rate divider which generated a pulse for every 100 events in the 0° detector. The "Master" and downscaled 0° signals were fed to a second CLU labeled "Master.Live," operated at a coincidence level of 1. The veto of the "Master.Live" CLU was fed by a "self-busy" signal which suppressed "Master.Live" signals when either the acquisition system or the CLU itself was already in operation. A "Master.Live" coincidence signified that a desired event had been detected, and was used to trigger the acquisition system. The "Master" and downscaled 0° logic signals were also fed to bits 1 and 2 of the acquisition system trigger bit register, respectively, indicating to the front and back end acquisition codes the type of event acquired. Where necessary, gate and delay generators (GDG) were used to produce proper logic signals.

Gates for ADCs were generated using GDGs fed directly by the "Master.Live" CLU. An additional CLU, requiring both a "Master.Live" event and a 0° detector event was used for generating start signals for time measurements and FERA gates. All TFCs and TDCs were started by 0° detector events. Times were measured for the beamline PIN diode, the cyclotron RF, both PPACs, the Si strips and the Si PINs. Since the events being timed occurred before the beam reached the 0°

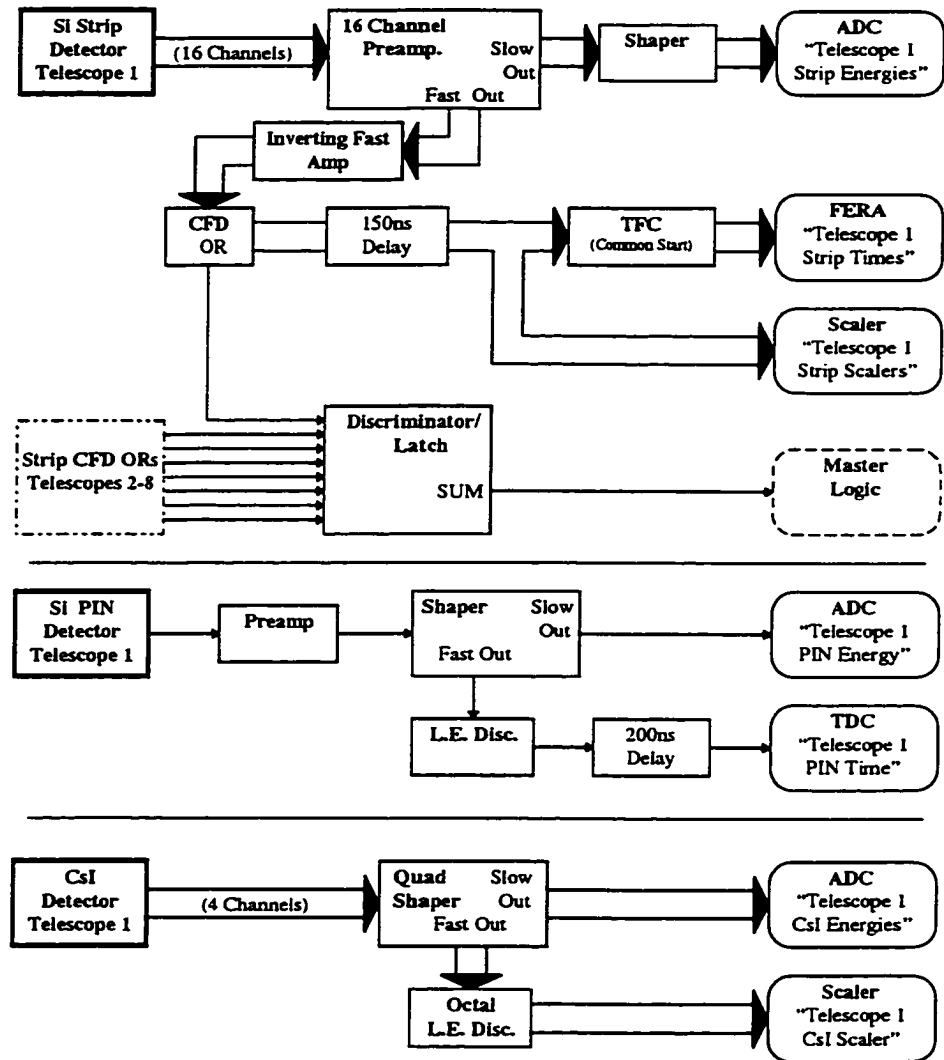


Figure 3.9: Electronics diagram for a single particle telescope. Gates and time starts were generated by the master electronics shown in Figure 3.11 and are not included explicitly here.

detector, cable delays (of 100-300 ns) were needed for signals used as stops in time measurements.

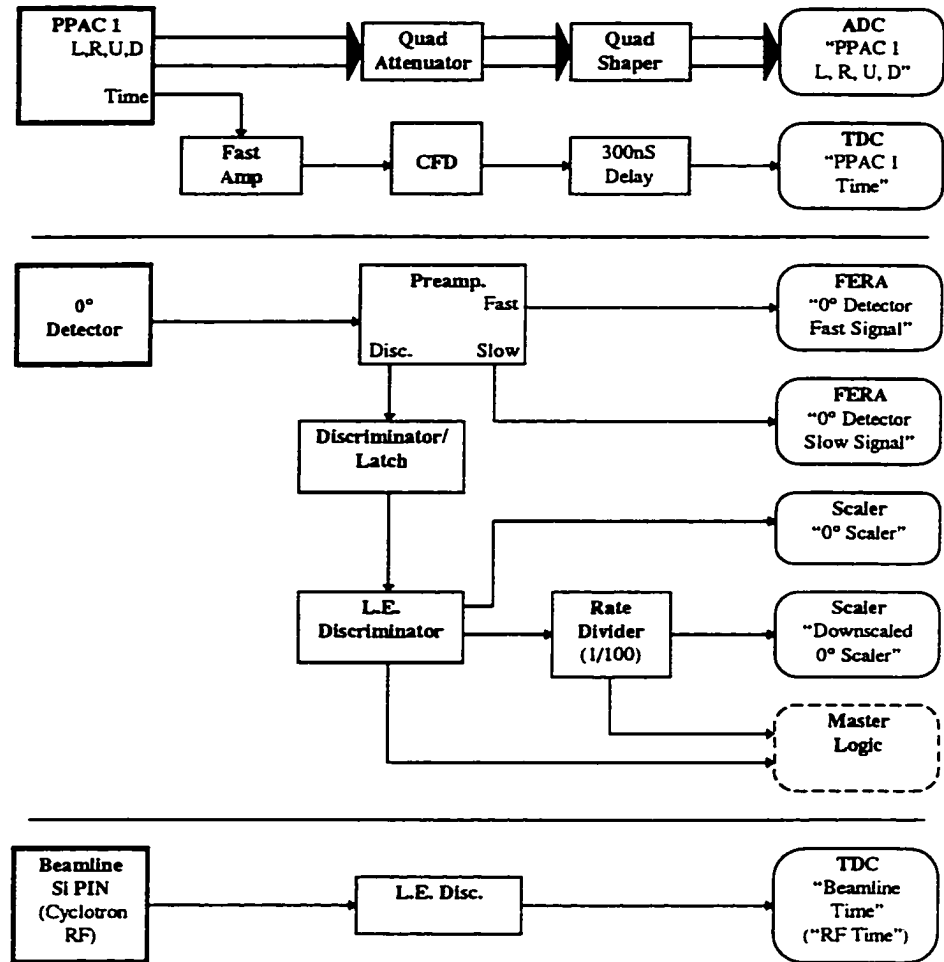


Figure 3.10: Electronics diagram for the beam detectors. Electronics for PPACs 1 and 2 were identical. Gates and time starts were generated by the master electronics shown in Figure 3.11 and are not included explicitly here.

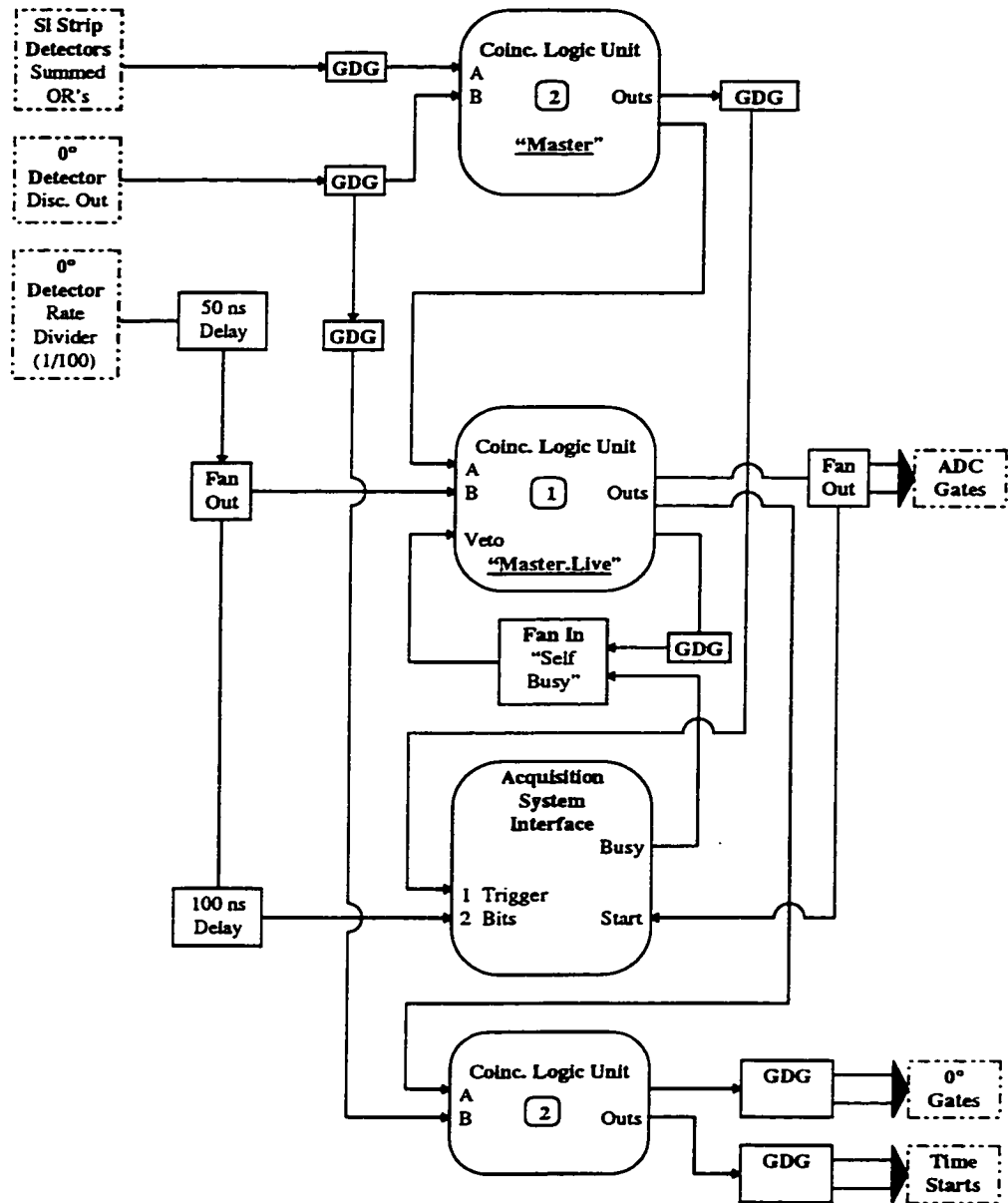


Figure 3.11: Diagram of the master electronics which generated event triggers and gates. The boxed number in the coincidence logic units indicates the coincidence level required between the two inputs labeled A and B.

CHAPTER 4

ANALYSIS AND RESULTS

4.1 Measurement of proton scattering angles

Figure 4.1, a vector diagram for an arbitrary inverse kinematics proton scattering event, is included to illustrate the measurement of proton scattering angles. For simplicity, the target is shown perpendicular to the beam in the figure. The target was actually mounted at an angle with respect to the beam about a vertical axis through its center as shown in Figures 3.2 and 4.4, and this is taken into account in beam tracking calculations. The particle telescopes are arranged such that the Si strips lie tangent to circles of constant θ_0 in a spherical coordinate system with its \hat{z} axis along the beamline optical axis and its origin at the center of the target (the optical alignment coordinate system). For a collimated beam, close to the optical axis, θ_0 , given by the location of the strip in which the proton is detected, is a good proton scattering angle measurement. Without collimation, beam particle trajectories are generally not parallel to the optical axis, nor are they incident on the target at its center, resulting in proton scattering angles $\theta \neq \theta_0$. However, if the trajectory of the incoming beam particle and the final position of the scattered proton are both known with respect to the optical alignment coordinate system, it is possible to calculate the position at which the scattering occurred as well as the proton scattering angle, θ .

We use left handed Cartesian optical alignment coordinates with the \hat{y} axis pointing down in the laboratory (see Figure 4.1). If the incoming beam particle has position $\vec{r}_1 = (x_1, y_1, z_1)$ at PPAC 1 and position $\vec{r}_2 = (x_2, y_2, z_2)$ at PPAC 2, where

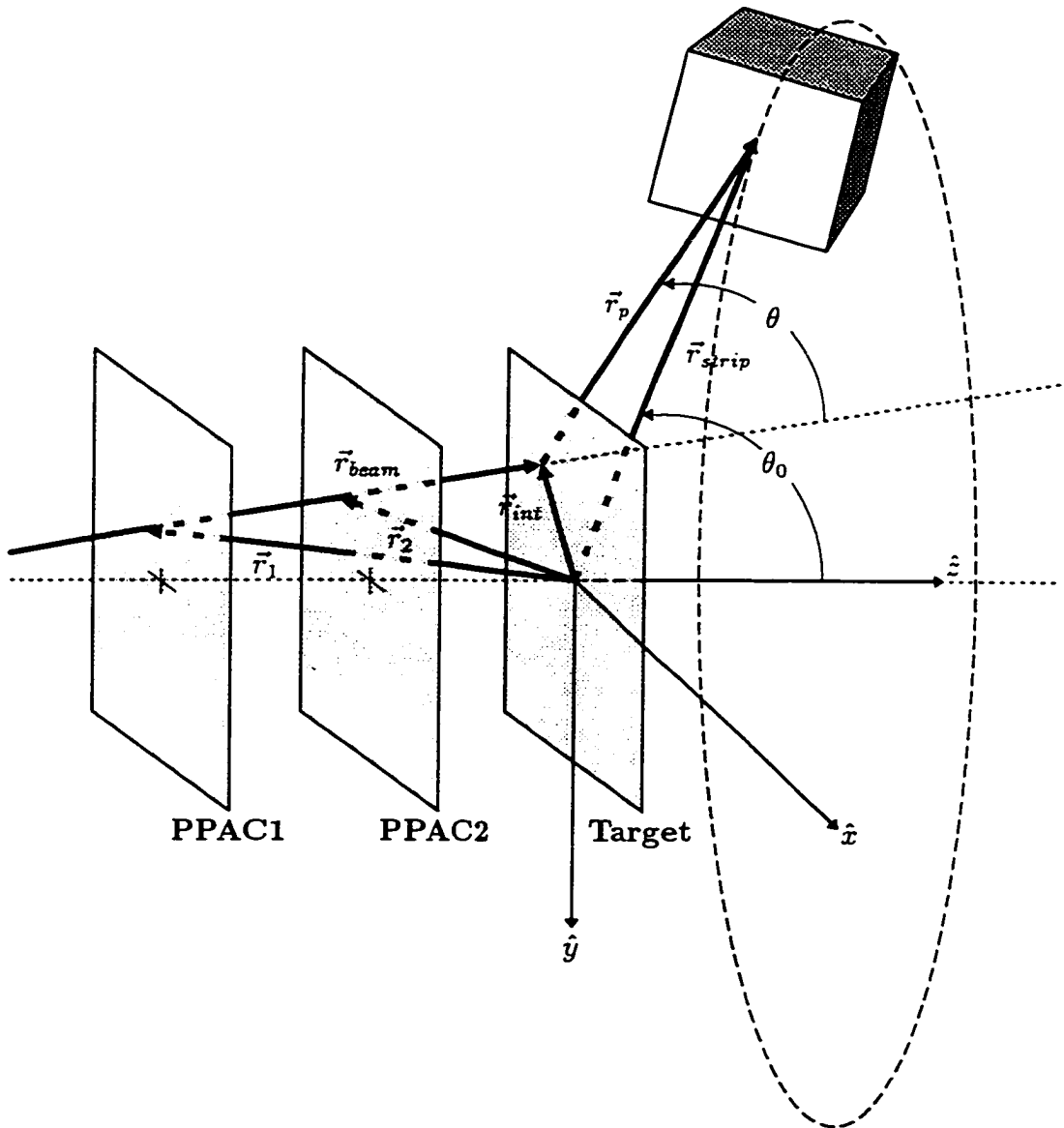


Figure 4.1: An arbitrary proton scattering event. The incoming beam particle with trajectory \vec{r}_{beam} is detected by the position sensitive PPACs at positions \vec{r}_1 and \vec{r}_2 and interacts with a proton in the target at position \vec{r}_{int} . The scattered proton is detected by a Si strip detector at an angle θ_0 , with respect to the optical axis, \hat{z} . The scattered proton trajectory, \vec{r}_p , is at an angle θ , the proton laboratory scattering angle, with respect to the incoming beam trajectory. For simplicity, the target is not shown at an angle with respect to the optical axis.

z_1 and z_2 are the fixed positions of the PPACs along the optical axis with respect to the target, the angle, θ_{beam} , of the beam trajectory with respect to the optical axis is given by

$$\theta_{beam} = \tan^{-1} \left(\frac{\sqrt{(x_2 - x_1)^2 + (y_2 - y_1)^2}}{|z_2 - z_1|} \right). \quad (4.1)$$

For a target rotated about the \hat{y} axis to an angle ψ with respect to the \hat{z} axis, the position of the intersection of the beam particle and the target (the point of interaction), \vec{r}_{int} , is given by

$$z_{int} = \frac{x_2 - \frac{\Delta x}{\Delta z} z_2}{\tan \psi - \frac{\Delta x}{\Delta z}} \quad (4.2)$$

$$x_{int} = x_2 + \frac{\Delta x}{\Delta z} (z_{int} - z_2) \quad (4.3)$$

$$y_{int} = y_2 + \frac{\Delta y}{\Delta z} (z_{int} - z_2) \quad (4.4)$$

$$(4.5)$$

where $\vec{\Delta} = \vec{r}_2 - \vec{r}_1$ describes the change in beam position between the two PPACs. The scattered proton is detected by a Si strip with its center at the known position \vec{r}_{strip} . The two vectors \vec{r}_{beam} and \vec{r}_p , describing the trajectories of the beam and the scattered proton, respectively, are given by

$$\vec{r}_{beam} = \vec{\Delta} \quad (4.6)$$

$$\vec{r}_p = \vec{r}_{strip} - \vec{r}_{int}. \quad (4.7)$$

The proton scattering angle, θ , the quantity of physical interest here, is the angle between them, which can be found from their scalar product as follows,

$$\theta = \cos^{-1} \left(\frac{\vec{r}_{beam} \cdot \vec{r}_p}{|\vec{r}_{beam}| |\vec{r}_p|} \right). \quad (4.8)$$

Figures 4.2 and 4.3 are representative beam tracking spectra. Two dimensional transverse position spectra measured by the PPACs are shown in Figure 4.2 along

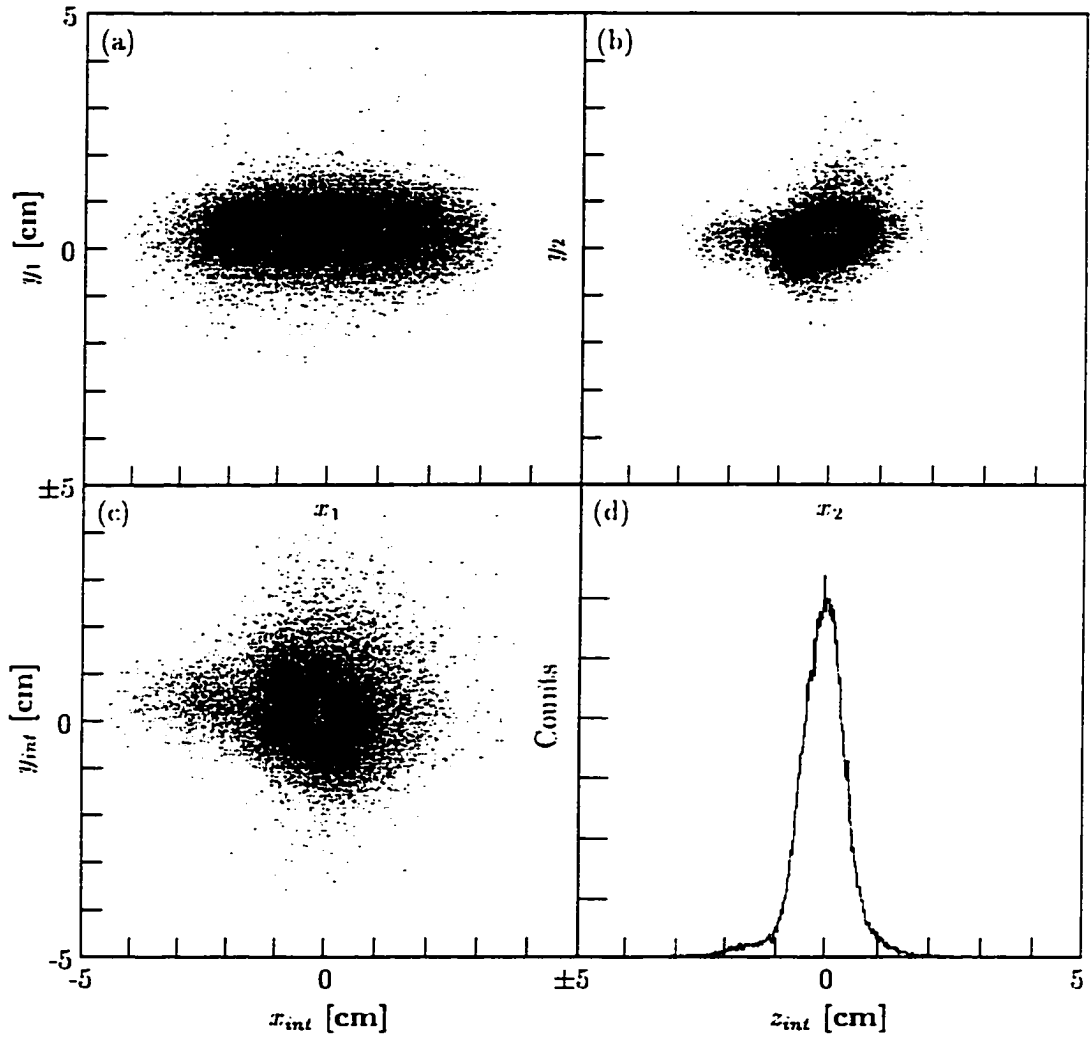


Figure 4.2: Beam tracking spectra. Two dimensional position spectra for the beam measured at (a) PPAC 1 and (b) PPAC 2, and the projected (c) transverse position and (d) z position spectra on target.

with the projected transverse and z position spectra on target. The nearly circular transverse profile of the beam on target had a full width at half maximum (FWHM) of 1.4 cm in \hat{x} and 1.3 cm in \hat{y} . The θ_{beam} spectrum appearing in Figure 4.3 has a FWHM of 0.9° .

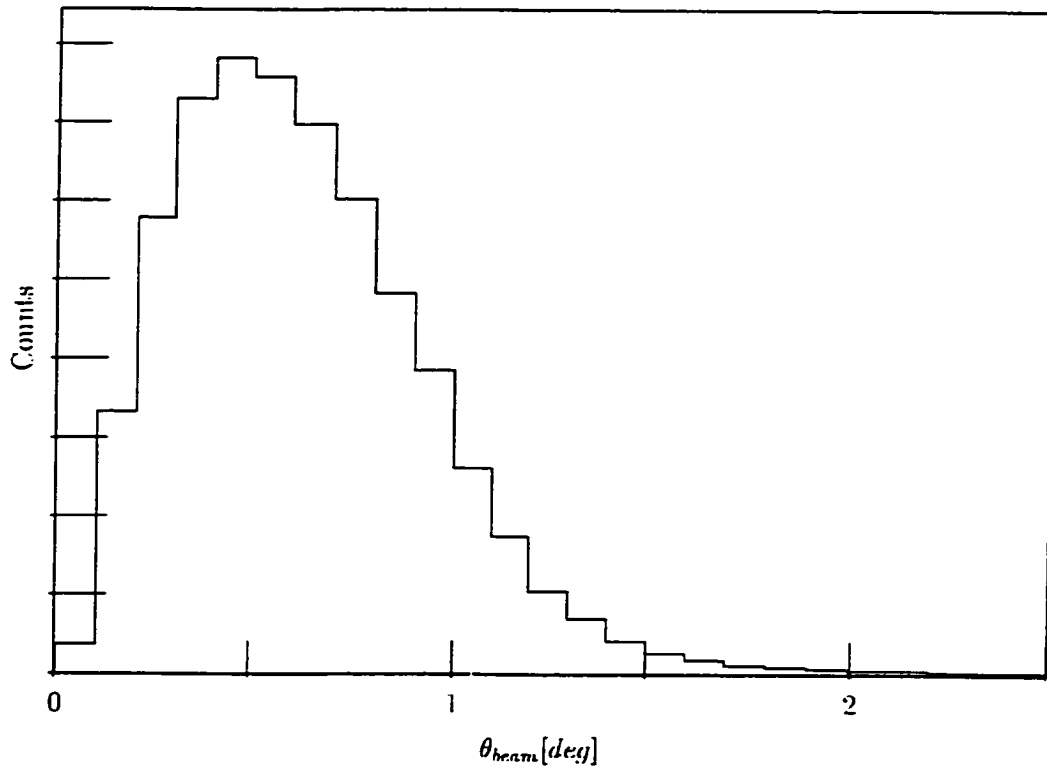


Figure 4.3: Beam divergence spectrum. The FWHM is 0.9° .

The target tilt of $\psi = 55^\circ$ was such that the region of beam interaction on target presented a much larger profile to telescopes 1-3 than to telescopes 5-7, resulting in a much larger spread in measured scattering angles for the former relative to the latter. An illustration of this effect, with exaggerated scale, is shown in Figure 4.4, in which the maximum angular size of the beam spot for telescopes 1-3 and 5-7 are labeled $\delta\theta_{1-3}$ and $\delta\theta_{5-7}$, respectively. The spectrum of deviations of measured scattering angles from the angular positions of the Si strips in the optical alignment system, given by $\Delta\theta = \theta - \theta_0$, for telescopes 5-7 in Figure 4.5(b) has a FWHM of 0.8° and a full width at tenth maximum (FWTM) of 2.1° . For a majority of events, the corrections are on the same order as the angular size of the strips and are therefore unnecessary.

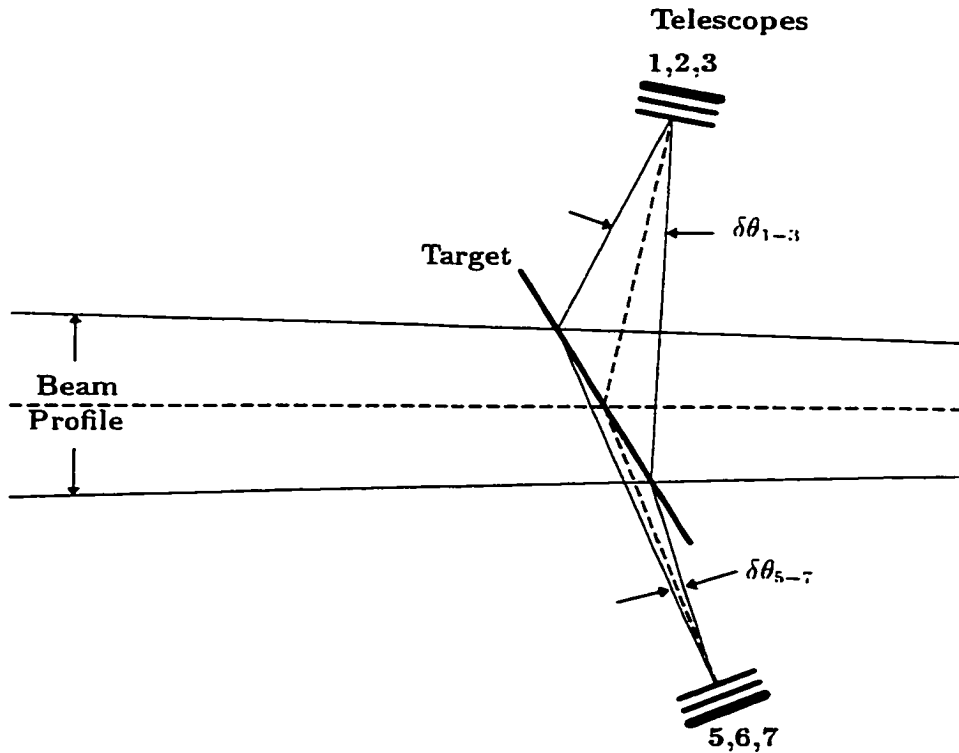


Figure 4.4: Illustration of the effects of target tilt on the spread in proton scattering angles, $\delta\theta$.

While the angular size of the beam spot as seen by the telescopes, $\delta\theta$ of Figure 4.4, does not take into account the angular divergence of the beam, and therefore $\delta\theta \neq \Delta\theta$, it is the dominant contribution to $\Delta\theta$ for telescopes 1-3. The beam tracking is essential in obtaining clear separation between elastic and inelastic scattering events for these telescopes. The $\Delta\theta$ spectrum (Figure 4.5(a)) for events in telescopes 1-3 has a FWHM of 4° and a FWTM of 8° . In effect, the beam divergence and the large beam profile on target expanded the angular field of view of each strip in these telescopes correspondingly.

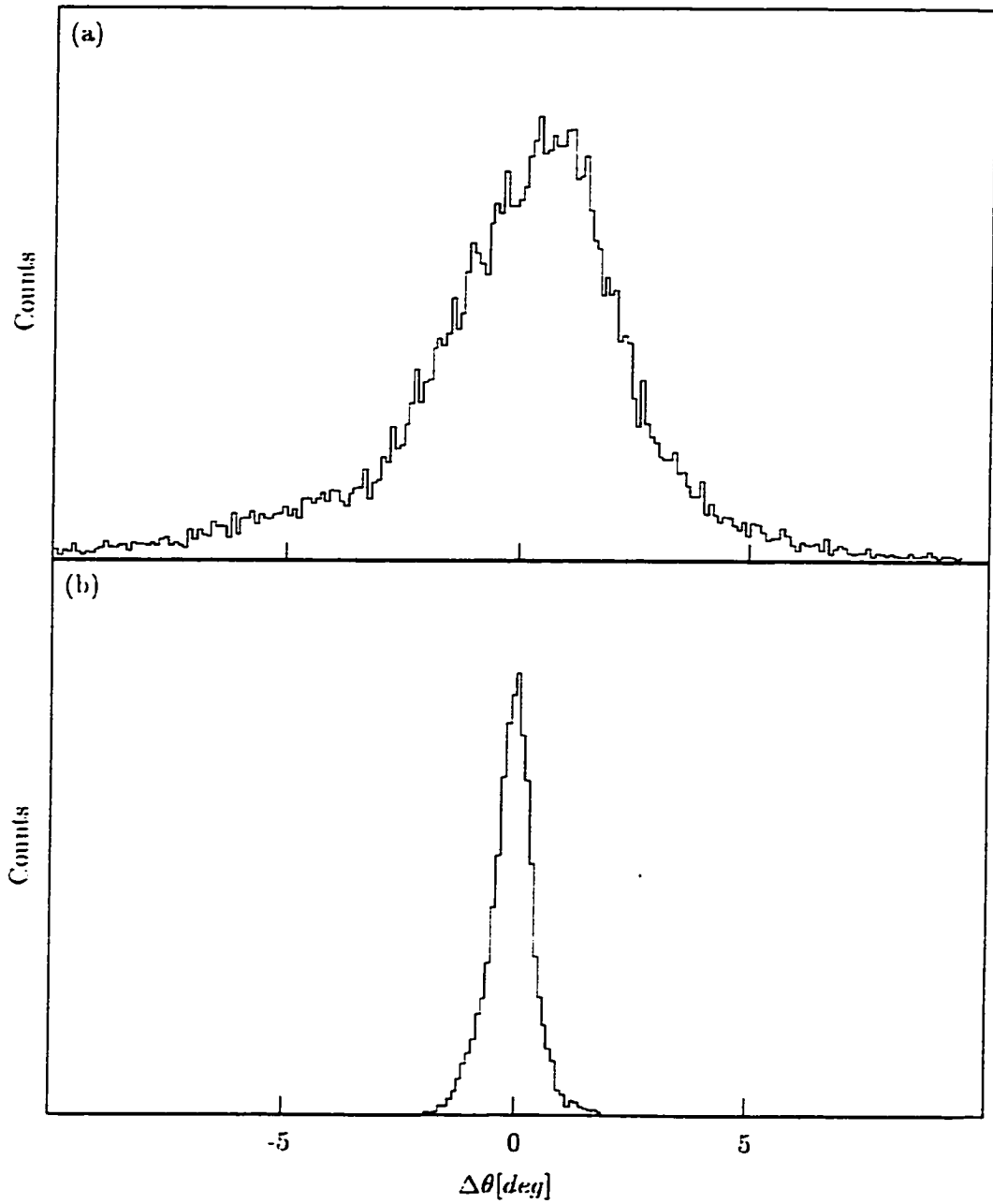


Figure 4.5: Scattering angle correction spectra for (a) telescopes 1-3 and (b) telescopes 5-7.

The statistical uncertainties in PPAC position measurements of 1 mm translate to an uncertainty in the transverse position of the beam on target of 1.4 mm, yielding an uncertainty in scattering angle corrections of 0.3° for telescopes 1-3 and 0.08° for telescopes 5-7. We estimate additional systematic errors, in the PPAC calibrations and the relative alignment of the PPACs, target and telescopes, to be on the order of $\pm 1^\circ$.

As is discussed below in Section 4.2, we generated proton angular distributions using the Si strips as bins. In order to keep the angular range of each point in the angular distribution to a reasonable size, we imposed an angular correction gate on events from telescopes 1-3, requiring $|\Delta\theta| \leq 1.5^\circ$ and thereby limiting the field of view of each strip to about 3.6° . With our angular correction gates, we rejected roughly 40% of the data from half of our particle telescopes, reducing our overall detection efficiency by about 20%.

It is useful at this point to compare the above mentioned loss of events due to large beam divergence in the present work to the loss we would have incurred had we collimated rather than tracked our beam. We are able to simulate beam collimation with software gates to obtain an estimate of the associated intensity loss. Square, 1 cm x 1 cm collimators at the PPAC positions (about 1 m and 2 m from the target) limit the beam divergence to $\theta_{beam} \leq 0.6^\circ$. The angular correction spectra for the collimated beam has a FWHM of 1.8° for telescopes 1-3 and 0.4° for telescopes 5-7, which corresponds to an acceptable angular resolution of the arrangement without beam tracking. These relatively large collimators allow roughly 15% of the total incident beam to reach the target. It should be noted that with beam tuning optimized for physical collimators, the loss would likely be more moderate. However, with the beam tracking correction to proton scattering angles, we were able to use 80% of the beam, while retaining acceptable angular resolution.

4.2 Proton angular distribution measurement

The proton scattering data used for the proton angular distribution measurement are presented in the form of a laboratory kinetic energy vs. scattering angle plot in Figure 4.6. The 10,764 events shown were measured in coincidence with both beam and proton identification gates and have been corrected for the large angular divergence and transverse profile of the beam as outlined in Section 4.1. The calculated kinematic curves for elastic scattering and scattering from the 1.89 MeV 2_1^+ state in ^{18}Ne are included for comparison. Since the field of view of telescopes 1-3 overlaps that of telescopes 5-7 in the angular range 70° - 75° , the detection efficiency of the telescope array is not homogeneous for the data shown. Clear separation between elastic and inelastic events is obtained. The absence of a significant background is also apparent. The data taken with the ^{12}C target yielded no evidence of any contributions to the proton data from the carbon in the polypropylene target.

The particle telescopes were mounted in sets of three, numbered 1-3 and 5-7, which shared the common geometric fields of view, $70^\circ - 80^\circ$ and $65^\circ - 75^\circ$, respectively (see Figures 3.2 and 3.8). The data from each set of three telescopes could be divided into 16 angular bins in the laboratory with gates on the parameter indicating which strip collected each proton event. These angular bins correspond to horizontal slices of the proton scattering data as presented in Figure 4.6. We used this natural binning of our data in the laboratory frame by the Si strips to generate the proton angular distributions of Figure 4.7. Summed proton laboratory kinetic energy vs. scattering angle spectra from each set of three telescopes, gated on a single strip number, are shown in Figure 4.8. Each point in the proton angular distributions, shown in Figure 4.7, corresponds to an intensity, for either elastic scattering or inelastic scattering to the 2_1^+ state, measured from a spectrum like those shown in Figure 4.8. Due to the lower inelastic yields, the inelastic points have been generated using pairs of adjacent strips. It should be noted that binning

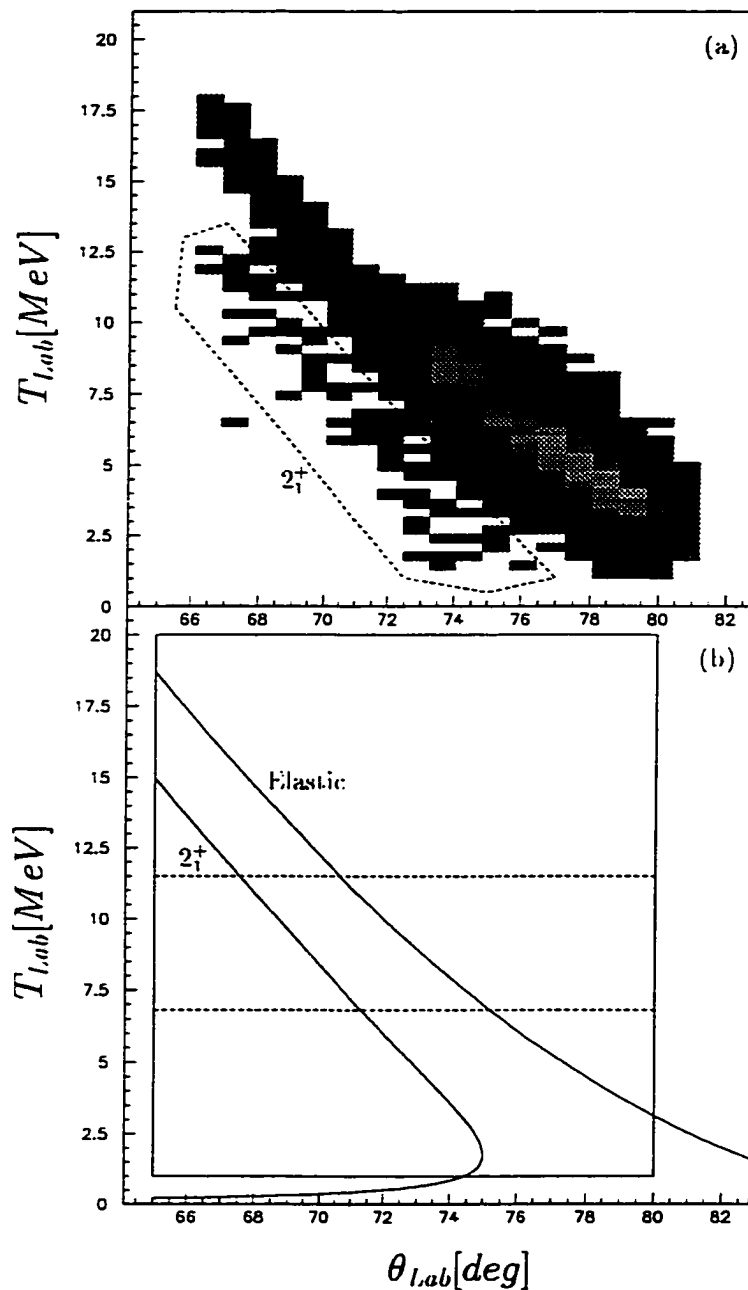


Figure 4.6: (a) Proton laboratory kinetic energy vs. scattering angle plot. The dashed outline indicates inelastic scattering events to the 2_1^+ state. (b) Calculated kinematics for comparison. The solid box represents the total geometrical field of view of the telescopes, with the dashed lines showing the divisions between the telescope layers. The lower energy limit of the telescope field of view is due to the noise thresholds of the Si strip detectors. The upper limit is not physically meaningful.

the data in the laboratory frame leads to a difference in scattering angles for elastic and inelastic points in the center of mass for each bin. The horizontal bars in Figure 4.7 correspond to the angular acceptance of the Si strips in the center of mass.

There were differences in overall detection efficiency between telescopes arising from problems with the acquisition electronics. We were therefore unable to measure absolute cross sections. The solid curves in Figure 4.7 are the result of a coupled channels (CC) calculation, described in detail in Section 2.3. We set the absolute cross section scale for the data by normalizing the measured proton intensities for a good fit to the calculated elastic cross sections. All of the strips in a given telescope were read out at once, and hence relative efficiencies between strips were unaffected by the electronics problems. An overall normalization was therefore applied to each telescope rather than to the individual strips.

Optical potential parameters, needed for the CC calculation, have not yet been deduced for ^{18}Ne . We rely on the assumption that parameters for elastic scattering do not vary greatly among neighboring nuclei and use the optical model parameters, listed in Table 2.2, deduced by de Swiniarski *et al.* [deS74] for the neighboring stable nucleus ^{20}Ne from elastic proton scattering cross sections measured at 30 MeV. The beam energy of the present work (30 MeV/u) gives the same center of mass energy as forward kinematics proton scattering at 30 MeV and was chosen with this analysis in mind.

After normalizing the measured proton intensities to the calculated elastic cross section curve, we varied the RMS quadrupole deformation parameter used in the CC calculation for a best fit to the measured elastic cross section, yielding a value of $\beta_2 = 0.46 \pm 0.04$. This variation had little effect on the calculated elastic cross section. We find overall good agreement between the data and the calculations.

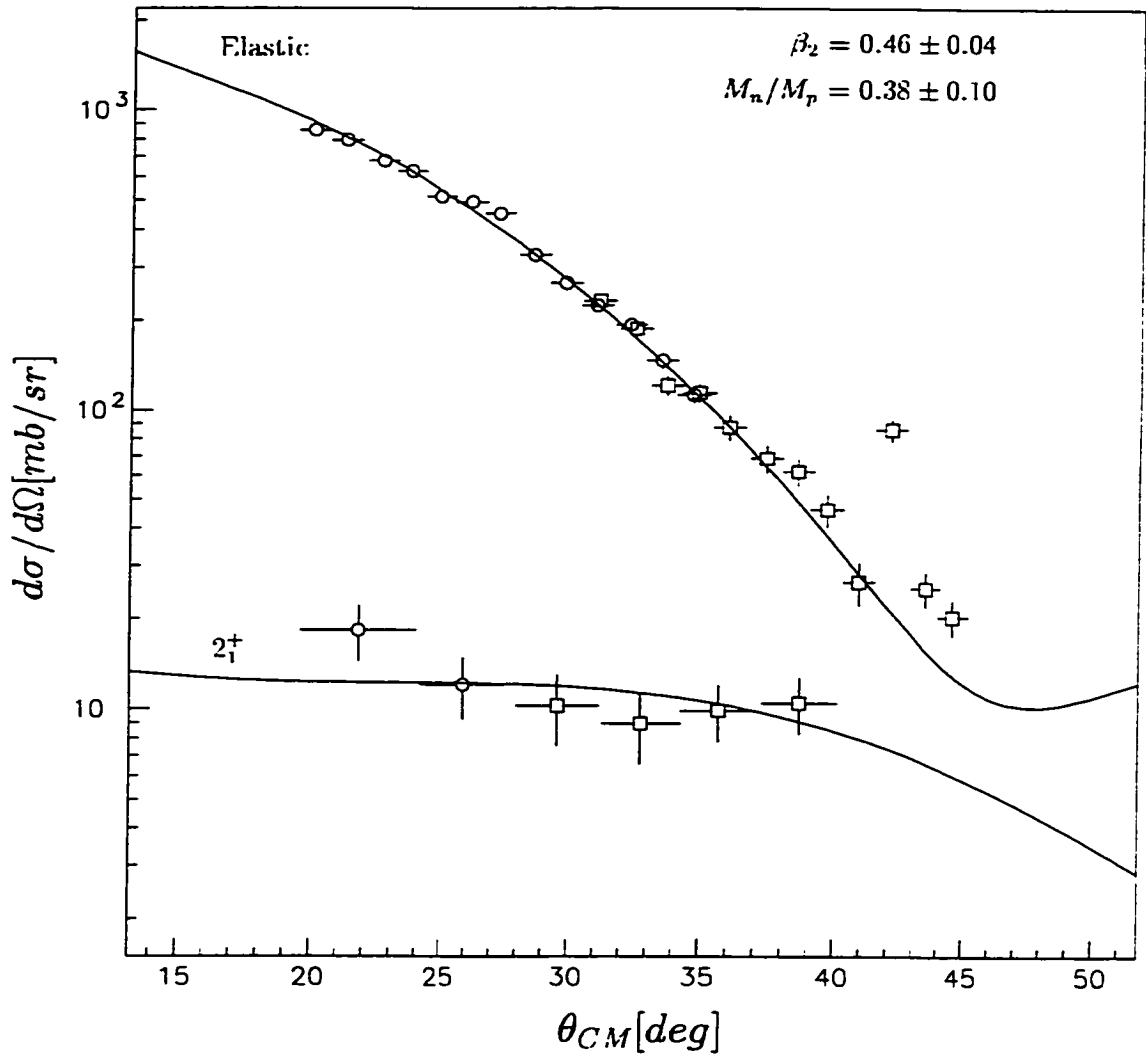


Figure 4.7: Measured and calculated angular distributions of protons scattered from the ground state and 2_1^+ state of ^{18}Ne . The circular points correspond to data from telescopes 1-3, and the square points are from telescopes 5-7. The horizontal bars indicate the angular field of view of the strip(s), and the vertical bars give the statistical uncertainties. The smooth curves are CC calculations using ^{20}Ne optical model parameters taken from [deS74] and the RMS quadrupole deformation β_2 giving the best fit to the inelastic cross sections. The corresponding M_n/M_p value is included.

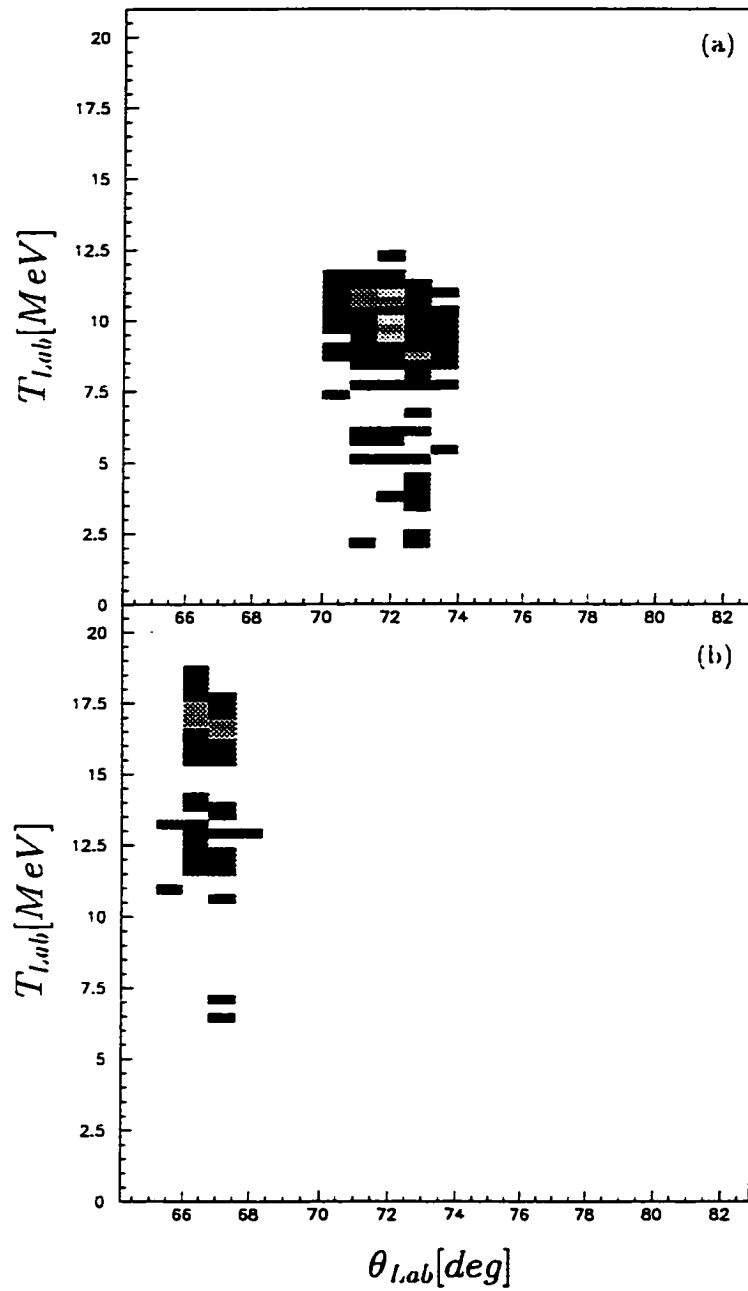


Figure 4.8: Summed proton laboratory kinematics spectra from (a) strips 4 of telescopes 1-3 and (b) strips 4 of telescopes 5-7.

4.3 The lifetime of the 2_1^+ state of ^{18}Ne

We take the electromagnetic β_2 value for the 2_1^+ state of ^{18}Ne from an existing γ ray lifetime, measured by McDonald *et al.* [McD76], using the Doppler shift attenuation method (DSAM), to which short lived states (≤ 1 ps) are accessible. In this method, excited nuclei are produced with velocities of at least a few percent of the speed of light, and emitted γ rays are detected as the recoiling nuclei are slowed and stopped by a thick target. Lifetimes on the order of the stopping time can then be deduced by analysis of the asymmetric broadening, due to Doppler shifting over a range of recoil velocities, of the energy peaks of the associated γ rays. The method requires information on the electronic and nuclear stopping powers, for the beam and the residual nucleus, of the target and stopping material used. The 2_1^+ state of ^{18}Ne was populated in the reaction $^3\text{He}(^{16}\text{O},n\gamma)^{18}\text{Ne}$. A projectile energy of 38 MeV, below the threshold for populating states above the 1.89 MeV 2_1^+ state, was chosen. Hence, no correction for feeding from higher lying levels was needed. A thick nickel stopping target, implanted with ^3He , was used. γ rays and neutrons were measured in coincidence at 0° . The mean lifetime of the 2_1^+ state of ^{18}Ne was determined to be 0.67 ± 0.07 ps.

The transition strength, or reduced transition probability, $B(E2)$, in units of the single particle estimate, known as Weisskopf units (W.u.), is related the mean lifetime of the nuclear state as follows,

$$B(E2) = \frac{\Gamma}{\Gamma_W} = \frac{\hbar/\tau}{4.9 \times 10^{-8} A^{4/3} E_\gamma^5} \quad (4.9)$$

where Γ and Γ_W are the experimentally determined and single particle natural line widths in eV, respectively, and E_γ is the transition energy in MeV. The reduced transition strength corresponding to the measured lifetime given above is $B(E2; 0_{gs}^+ \rightarrow 2_1^+) = 17.7 \pm 1.8$ W.u. Given that electromagnetic probes are sensitive solely to protons, this result indicates highly collective proton behavior. The RMS

quadrupole proton deformation is then given by [Ber69]

$$\beta_2 = \frac{\sqrt{20\pi B(E2)}}{5Z}, \quad (4.10)$$

yielding a value of 0.67 ± 0.07 .

4.4 Determination of M_n/M_p

We obtain M_n/M_p for the 1.89 MeV 2_1^+ state in ^{18}Ne by comparison of the RMS deformation lengths, δ_2^p and δ_2^{EM} deduced from the proton scattering angular distribution of the present work and from an existing γ ray lifetime measurement described below. These deformation lengths, given by $\delta_2 = \beta_2 r_0 A^{\frac{1}{3}}$, are the RMS amplitudes in fm of the quadrupole vibrations induced by the two probes. Both β_2 and r_0 are probe dependent. The differing sensitivities of these two probes are taken into account by the relation,

$$\frac{M_n}{M_p} = \frac{b_p^p}{b_n^p} \left[\frac{\delta_2^p}{\delta_2^{EM}} \left(1 + \frac{b_n^p N}{b_p^p Z} \right) - 1 \right], \quad (4.11)$$

obtained from Equation 2.15 with $F = p$ and $G = EM$. The relatively simple form of Equation 4.11 arises from the selectivity of electromagnetic measurements, $b_n^{EM}/b_p^{EM} = 0$. As discussed in Section 2.2, proton scattering in the 10-50 MeV range is approximately three times more sensitive to neutrons than protons, yielding $b_n^p/b_p^p = 3$. Using mean radius parameters r_0 of 1.10 fm for proton scattering, from the optical model parameters for ^{20}Ne (see Table 2.2), and the standard 1.20 fm for electromagnetic excitations [Ald56], we obtain $M_n/M_p = 0.38 \pm 0.10$.

CHAPTER 5

DISCUSSION

The result of the present work, $M_n/M_p = .38 \pm .10$ for the 1.89 MeV 2_1^+ state in ^{18}Ne , falls well below $N/Z = 0.8$, indicating a large isovector component to the excitation, or stated more simply, that protons dominate the 2_1^+ state. Given that the two valence nucleons in ^{18}Ne are protons, this is quite consistent with the picture of a relatively inert core comprised of the nucleons filling the $N = 8$ and $Z = 8$ major shells. Hence, it appears that we observe a large shell structure effect in this nucleus.

Ratios of M_n/M_p to N/Z for 2_1^+ states of nuclei in the $12 \leq A \leq 26$ mass region, including the result of the present work, are plotted in Figure 5.1. Results from comparisons of electromagnetic [Ram87], proton scattering [DeL83, Gra80, Je:diss, deS74, Has83, Zwi83] and neutron scattering [Ols89, Gra80, Ols90] measurements are included, where available. The nucleon scattering results are taken from sources in which coupled channels analyses similar to those of the present work have been used to extract RMS quadrupole deformation lengths. The value for ^{20}O was obtained from a measurement made with the same experimental arrangement and method of analysis as the present work [Je:diss]. In all cases, we extract M_n/M_p using Equation 2.15 with the probe sensitivities listed in Table 2.1. The reciprocals of the results for ^{18}O are also included in Figure 5.2 for comparison with the result of the present work for ^{18}Ne , its mirror partner.

As expected on the basis of the simple shell model argument given in Section 2.1, ^{18}Ne , with its closed $N = 8$ neutron shell has $(M_n/M_p)/(N/Z) < 1$, and ^{18}O and ^{20}O , with closed $Z = 8$ proton shells, have $(M_n/M_p)/(N/Z) > 1$. However, larger departures from $(M_n/M_p)/(N/Z) = 1$ in the open shell Ne and Mg isotopes than

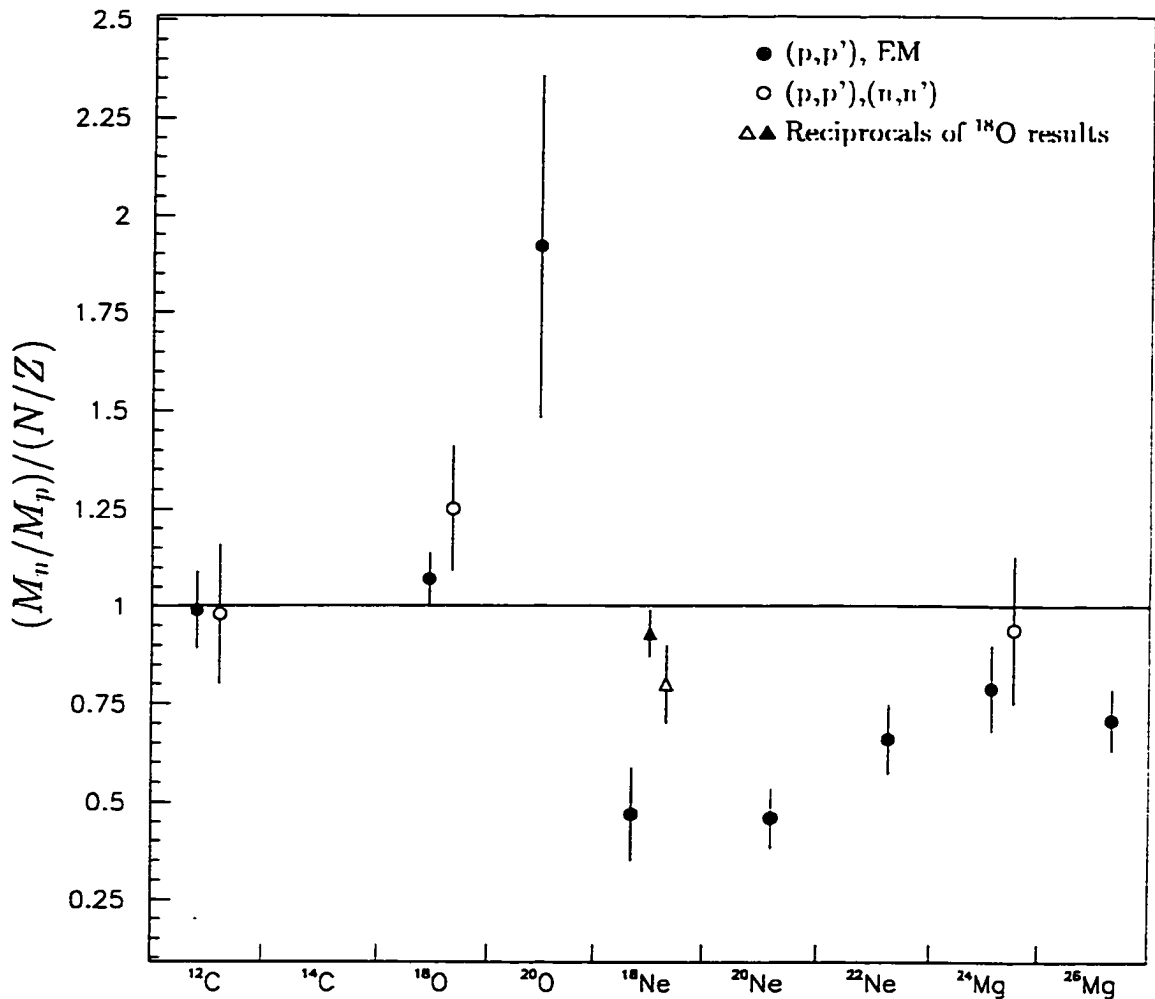


Figure 5.1: The ratio M_n/M_p to N/Z for the 2_1^+ states of nuclei in the $12 \leq A \leq 26$ mass region from comparisons of electromagnetic (EM) [Ram87], proton scattering [DeL83, Gra80, Je:diss, deS74, Has83, Zwi83] and neutron scattering [Ols89, Gra80, Ols90] measurements. The triangular points are the reciprocals of the result for ^{18}O , the mirror partner of ^{18}Ne .

in the SCS nucleus ^{18}O are also present. The prediction, due to isospin symmetry, of Equation 1.3, that $M_{n(p)}(^{18}\text{Ne}) = M_{p(n)}(^{18}\text{O})$ is not supported by these measurements. In the cases for which low energy inelastic neutron scattering measurements

exist, good agreement is found between the EM vs. proton scattering and proton scattering vs. neutron scattering methods of obtaining M_n/M_p .

As outlined in Section 2.2 pion scattering in the energy region of the $\Delta(P_{33})$ resonance is an independent method of obtaining M_n/M_p . In Figure 5.2, we compare the available pion scattering results in the mass region, compiled by Peterson, [Pet93] to the EM and nucleon results presented in Figure 5.1. We were unable to find low energy inelastic nucleon scattering data for ^{14}C , but we include the pion scattering result in the figure, because it is an SCS nucleus. The pion scattering results follow the predictions of the simple shell model, showing the appropriate deviations from $M_n/M_p = N/Z$ for ^{14}C and ^{18}O , and fall close to the collective model prediction of N/Z for the open shell nuclei. The quantitative agreement between pion scattering results and those involving nucleon scattering is rather poor for the stable oxygen and neon isotopes, but the qualitative feature of a large neutron contribution in ^{18}O , relative to ^{18}Ne and its open shell neighbors, is seen for both sets of results.

On the basis of simple shell model and collective model arguments, the pion scattering results of Figure 5.2 seem quite reasonable, and the proton scattering vs. electromagnetic (PEM) results seem suspect. However, in a more realistic picture of nuclear structure effects in the mass region, the evaluation of the two methods is not as straightforward. Results of the shell model calculations, including core polarization, of Brown *et al.* [Bro82] described in Section 2.2, for ^{18}O , ^{18}Ne , ^{20}Ne and ^{26}Mg are also presented in Figure 5.2. Experimental PEM and pion scattering results exist for the stable nuclei for which calculations exist, and in each case, the calculation falls between the two. We conclude, in light of the measurements and calculations presented here, that there are isovector components, consistent with shell closure effects, to the 2_1^+ states of both ^{18}Ne and ^{18}O . Despite the apparent success of the methods used here for mainly $A > 40$ SCS nuclei [Ber81], whether

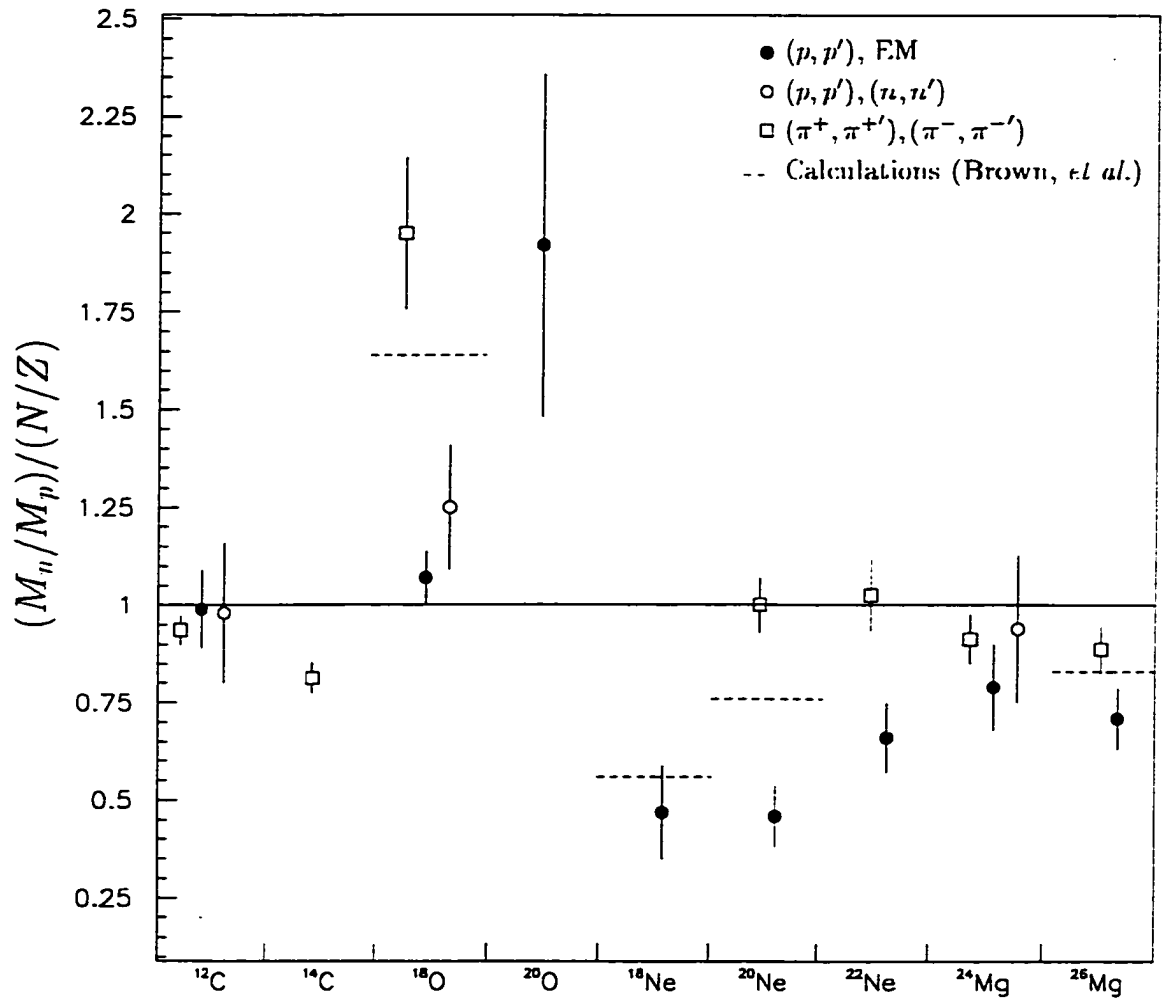


Figure 5.2: The ratio M_n/M_p to N/Z for the 2_1^+ states of nuclei in the $12 \leq A \leq 26$ mass region. Pion scattering results [Pet93] are included along with the electromagnetic and nucleon scattering results of Figure 5.1. Dashed lines are calculations from [Bro82].

we have obtained absolute measurements of M_n/M_p in this mass region remains an open question.

The differences between M_n/M_p as determined by PEM and nucleon scattering methods and those obtained from pion scattering are possibly due to the fact that we

have not completely removed the probe dependence from our results in the formalism leading to Equation 2.15. It is perhaps not surprising that pion scattering at 200 MeV, which probes the nuclear interior, gives a different answer than low energy nucleon scattering, which is sensitive mainly to the nuclear surface [Ost79, Car85]. Differences in the analyses of nucleon and pion scattering cross sections may also lead to a systematic difference between the two methods having little to do with the structure of the target nucleus. The pion scattering results presented here [Pet93] are taken from a single collection for which a consistent distorted wave impulse approximation (DWIA) analysis was used. It would be useful to compile a similar consistent analysis of all of the nucleon scattering data in the mass region.

Wider experimental coverage of $N = 8$ and $Z = 8$ SCS nuclei is also of interest. Inverse kinematics proton scattering requires a beam intensity of at least a few thousand pps, and Coulomb excitation measurements can be made with only a few pps. Both of these measurements are currently feasible for the $N = 8$ SCS nucleus ^{12}Be , with a beam intensity from primary fragmentation at the NSCL, estimated with the computer code INTENSITY [Win92], of $\approx 20,000$ pps. The calculated estimate for ^{20}Mg , the mirror partner of ^{20}O and thus of particular interest, is ≈ 1 pps, and the possible beam intensities for ^{22}O and ^{24}O have been determined experimentally [Fa:diss] to be ≈ 300 pps and ≈ 1 pps, respectively. All three of these nuclei are currently, in principle, accessible by Coulomb scattering measurements. The planned upgrade of the accelerator facility at the NSCL, involving the coupling of the K1200 and K500 superconducting cyclotrons and the installation of an improved A1900 beam analysis system, will bring an estimated factor of 10,000 increase in beam yields for these light secondary beams, placing them within the reach of inverse kinematics proton scattering measurements as well. The estimated completion date of the upgrade project is spring of 2000.

CHAPTER 6

SUMMARY

The first inelastic proton scattering measurement for a proton rich nucleus heavier than $A = 3$, performed in inverse kinematics with a radioactive ^{18}Ne beam, has been carried out at the NSCL at MSU. The RMS quadrupole deformation length, δ_2 , of the 1.89 MeV 2_1^+ state in ^{18}Ne has been extracted with a coupled channels analysis from the measured inelastic proton angular distribution. In combination with a δ_2 for protons deduced from an existing γ ray lifetime measurement [McD76], a value of $M_n/M_p = 0.38 \pm .10$ is obtained. This result is over a factor of two less than $N/Z = 0.8$, indicating a large isovector component to the 2_1^+ collective quadrupole vibration in ^{18}Ne . This result is consistent with a picture of two valence protons, which dominate the excitation, outside relatively inert filled $N = 8$ neutron and $Z = 8$ proton shells. Our result for ^{18}Ne is also qualitatively consistent with the neutron dominance observed in the 2_1^+ state of its mirror partner, ^{18}O , in which $Z = 8$.

A comparison of M_n/M_p for 2_1^+ states in even-even nuclei in the $12 \leq A \leq 26$ mass region, as determined using electromagnetic, 10-50 MeV nucleon scattering, and 160-200 MeV pion scattering measurements has revealed a systematic difference between values obtained using nucleon scattering and those obtained from pion scattering for nuclei near the $N = 8$ and $Z = 8$ shell closures. We suggest that a more consistent method of analysis of the nucleon scattering data in the mass region and further measurements in $N = 8$ and $Z = 8$ SCS nuclei may help to resolve these discrepancies.

APPENDIX

APPENDIX

MEASURED CROSS SECTIONS

The following tables show the cross sections, plotted in Figure 4.7, determined by scaling the measured proton intensities to fit elastic cross sections from the coupled channels calculations described in Section 2.3. The uncertainties in scattering angles correspond to the geometrical fields of view of the Si strips in the laboratory, and the uncertainties listed for the cross sections are statistical. Cross sections from telescopes 1-3 are listed in Table A.1, and those from telescopes 5-7 are listed in Table A.2.

Table A.1: Measured proton cross sections from the reaction ${}^1\text{H}({}^{18}\text{Ne}, {}^{18}\text{Ne}')\text{p}$ at 30 MeV/u taken from particle telescopes 1-3.

Strip #	θ_{Lab} [deg]	θ_{CM} [deg]	$d\sigma/d\Omega$ [mb/sr]
Telescopes 1,2 & 3 Elastic			
4	72.2±0.3	34.7±0.6	112 ± 7
5	72.8	33.5	146 ± 9
6	73.4	32.3	193 ± 10
7	74.1	31.0	224 ± 11
8	74.7	29.8	265 ± 12
9	75.3	28.6	327 ± 14
10	76.0	27.2	452 ± 16
11	76.6	26.1	494 ± 17
12	77.2	24.9	515 ± 18
13	77.8	23.7	624 ± 20
14	78.4	22.6	674 ± 22
15	79.1	21.2	791 ± 24
16	79.7	20.0	856 ± 27
Telescopes 1,2 & 3 2_1^+			
4,5	72.5 ± 0.6	25.9 ± 1.7	12 ± 3
6,7	73.8	21.8 ± 2.2	18 ± 4

Table A.2: Measured proton cross sections from the reaction ${}^1\text{H}({}^{18}\text{Ne}, {}^{18}\text{Ne}')\text{p}$ at 30 MeV/u taken from particle telescopes 5-7.

Strip #	θ_{Lab} [deg]	θ_{CM} [deg]	$d\sigma/d\Omega$ [mb/sr]
Telescopes 5,6 & 7 Elastic			
4	67.1±0.3	44.6±0.6	20 ± 3
5	67.7	43.5	25 ± 3
6	68.4	42.1	86 ± 8
7	69.0	40.9	26 ± 4
8	69.6	39.7	46 ± 6
9	70.2	38.6	62 ± 7
10	70.8	37.4	68 ± 7
11	71.5	36.0	87 ± 8
12	72.1	34.9	114 ± 8
13	72.7	33.7	121 ± 9
14	73.3	32.5	187 ± 11
15	74.0	31.1	231 ± 12
Telescopes 5,6 & 7 2_1^+			
4,5	67.4±0.6	38.7±1.4	10 ± 2
6,7	68.7	35.7±1.4	10 ± 2
8,9	69.9	32.8±1.5	9 ± 2
10,11	71.2	29.6±1.6	10 ± 3

BIBLIOGRAPHY

- [Ald56] K. Alder, A. Bohr, T. Huus, B. Mottelson, A. Winther, *Rev. Mod. Phys.* **28**, 432 (1956).
- [Ann87] R. Anne, D. Bazin, A.C. Mueller, J.C. Jacmart, M. Langevin, *Nucl. Instr. and Meth.* **A257**, 215 (1987).
- [Ann95] R. Anne, D. Bazin, R. Bimbot, M.J.G. Borge, J.M. Corre, S. Dogny, S. Emling, D. Guillemaud-Mueller, P.G. Hansen, P. Hornshj, P. Jensen, B. Johnson, M. Lewitowicz, A.C. Mueller, R. Neugart, T. Nilsson, G. Nyman, F. Pougheon, M.G. Saint-Laurent, G. Schreider, O. Sorlin, O. Tengblad, K. Wilhelmsen-Rolander, *Z. Phys.* **A352**, 397 (1995).
- [Bal47] G.C. Baldwin, G.S. Klaiber, *Phys. Rev.* **71**, 3 (1947).
- [Bal48] G.C. Baldwin, G.S. Klaiber, *Phys. Rev.* **73**, 1156 (1948).
- [Ber69] A.M. Bernstein, in *Advances in Nuclear Physics*, M. Baranger, E. Vogt, ed., Vol. 3, Plenum, New York (1969).
- [Ber79] A.M. Bernstein, V.R. Brown, V.A. Madsen, *Phys. Rev. Lett.* **42**, 425 (1979).
- [Ber81] A.M. Bernstein, V.R. Brown, V.A. Madsen, *Phys. Lett.* **103B**, 255 (1981).
- [Ber83] A.M. Bernstein, V.R. Brown, V.A. Madsen, *Comments Nucl. Part. Phys.* **11**, 203 (1983).
- [Bla79] J.M. Blatt, V.F. Weisskopf, *Theoretical Nuclear Physics*, Springer-Verlag, New York (1979).

- [Boh39] N. Bohr, J.A. Wheeler, *Phys. Rev.* **56**, 426 (1939).
- [Boh52] A. Bohr, *Kgl. Dan. Mat. Fys. Medd.* **26** no. 14 (1952).
- [Boh53] A. Bohr, B.R. Mottelson, *K. Danske Vidensk. Selsk. Mat.-Fys. Medd.* **27** no. 16 (1953).
- [Boh69] A. Bohr, B.R. Mottelson, *Nuclear Structure, Vol. I*, W.A. Benjamin, Inc., Reading, Massachusetts (1969).
- [Boh75] A. Bohr, B.R. Mottelson, *Nuclear Structure, Vol. II*, W.A. Benjamin, Inc., Reading, Massachusetts (1975).
- [Bro59] G.E. Brown, M. Bosterli, *Phys. Rev. Lett.* **10**, 472.
- [Bro80] B.A. Brown, B.H. Wildenthal, *Phys. Rev.* **C21**, 2107 (1980).
- [Bro80b] B.A. Brown, W. Chung, B.H. Wildenthal, *Phys. Rev.* **C21**, 2600 (1980).
- [Bro82] B.A. Brown, B.H. Wildenthal, W. Chung, S.E. Massen, M. Bernas, A.M. Bernstein, R. Miskimen, V.R. Brown, V.A. Madsen, *Phys. Rev.* **C26**, 2247 (1982).
- [Bro75] V.R. Brown, V.A. Madsen, *Phys. Rev.* **C11**, 1298 (1975).
- [Bro61] G.E. Brown, L. Castillejo, J.A. Evans, *Nucl. Phys.* **22**, 1 (1961).
- [Car85] J.A. Carr, F. Petrovich, J.J. Kelly, in *Neutron-Nucleus Collisions: A Probe of Nuclear Structure*, AIP Conf. Proc. No. 124, ed. J.Rapaport, R.W.Finlay, S.M.Grimes, and F.S.Dietrich, AIP, New York (1985).
- [Comf] J.R. Comfort, University of Pittsburgh report (unpublished).
- [DeL83] R. De Leo G. D.'Erasmus, A. Pantaleo, M.N. Harakeh, E. Cereda, S. Micheletti, M. Pignanelli, *Phys. Rev.* **28**, 1443 (1983).

- [deS74] R. de Swiniarski, A. Genoux-Lubain, G. Bagieu, J.F. Cavaignac, *Can. J. Phys.* **52**, 2422 (1974).
- [Eis80] J.M. Eisenberg, D.S. Koltun, *Theory of Meson Interactions with Nuclei*, John Wiley and Sons, New York, (1980).
- [Fa:diss] M. Fauerbach, Ph.D. Dissertation, Michigan State University (1997).
- [Fee49] E. Feenberg, *Phys. Rev.* **75** 320 (1949).
- [Flu41] S. Flügge, *Ann. Phys.* **39**, 373 (1941).
- [Fox89] R. Fox, R. Au, A. VanderMolen, *IEEE Trans. Nucl. Sci.*, 1562 (1989).
- [Gam29] G. Gamow, *Roy. Soc. Proc.* **A123**, 386 (1929).
- [Gei95] H. Geissel, G. Münzenberg, K. Riisager, *Ann. Rev. Nucl. Part. Sci.*, **45**, 163 (1995).
- [Gol48] M. Goldhaber, E. Teller, *Phys. Rev.* **74**, 1046 (1948).
- [Gor49] W. Gordy, *Phys. Rev.* **76**, 139 (1949).
- [Gra80] P. Grabmayr, J. Rapaport, R.W. Finlay, *Nucl. Phys.* **A350**, 167 (1980).
- [Hah96] K.I. Hahn, A. Garcia, E.G. Adelberger, P.V. Magnus, A.D. Bacher, N. Bateman, G.P.A. Berg, J.C. Blackmon, A.E. Champagne, B. Davis, A.J. Howard, J. Liu, B. Lund, Z.Q. Mao, D.M. Markoff, P.D. Parker, M.S. Smith, E.J. Stephenson, K.B. Swartz, S. Utku, R.B. Volegaar, K. Yildiz, *Phys. Rev.* **C54**, 1999 (1996).
- [Has83] D.K. Hassell, N.E. Davison, T.N. Nasr, B.T. Murdoch, A.M. Sourkes, W.T.H. van Oers, *Phys. Rev.* **C27**, 482 (1983).
- [Hei32] W. Heisenberg, *Z. Phys.* **77**, 1 (1932).

- [Je:diss] J.K. Jewell, Ph.D. Dissertation, Florida State University (1997).
- [Kel97] J.H. Kelley, T Suomijärvi, S.E. Hirzebruch, A. Azhari, D. Bazin, Y. Blumenfeld, J.A. Brown, P.D. Cottle, S. Danczyk, M. Fauerbach, T. Glasmacher, J.K. Jewell, K.W. Kemper, F. Maréchal, D.J. Morrissey, S. Ottini, J.A. Scarpaci, P. Thirolf, submitted to *Phys. Rev. Lett.* (1997).
- [Ken56] H. Kendall, L. Grodzins, *Bull. Am. Phys. Soc.* **1**, (1956).
- [Ken92] M.A. Kennedy, P.D. Cottle, K.W. Kemper, *Phys. Rev.* **C46**, 1811 (1992).
- [Kno79] G.F. Knoll, *Radiation Detection and Measurement*, John Wiley and Sons, New York (1979).
- [Kra94] G. Kraus, P. Egelhof, C. Fischer, H. Geissel, A. Himmler, F. Nickel, G. Münzenberg, W. Schwab, A. Weiss, J. Friese, A. Gillitzer, H.J. Körner, M. Peter, W.F. Henning, J.P. Schiffer, J.V. Kratz, L. Chulkov, M. Golovkov, A. Ogloblin, B.A. Brown, *Phys. Rev. Lett.* **73**, 1773 (1994).
- [Kunz] P.D. Kunz, University of Colorado report (unpublished).
- [Mad75] V.A. Madsen, V.R. Brown, J.D. Anderson, *Phys. Rev.* **C12**, 1205 (1975).
- [Mad84] V.A. Madsen, V.R. Brown, *Phys. Rev. Lett.* **52**, 176 (1984).
- [May48] M.G. Mayer, *Phys. Rev.* **74**, 235 (1948).
- [May49] M.G. Mayer, *Phys. Rev.* **75**, 1969 (1949).
- [McD76] A.B. McDonald, T.K. Alexander, C. Broude, J.S. Forster, O. Häuser, F.C. Khanna, I.V. Mitchell, *Nucl. Phys.* **A258**, 152 (1976).
- [Mor87] C.L. Morris, S.J. Seestrom-Morris, D. Dehnhard, C.L. Blilie, R. Gilman, G.P. Gilfoyle, J.D. Zunbro, M.G. Burlein, S. Mordechai, H.T. Fortune, L.C.

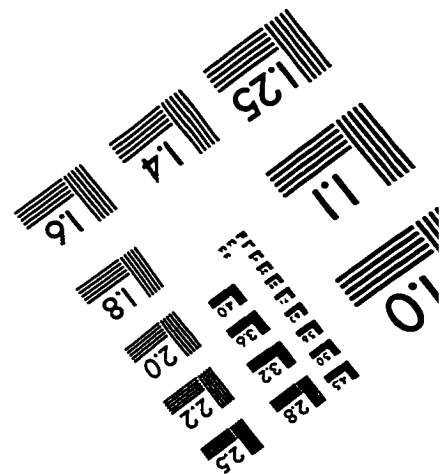
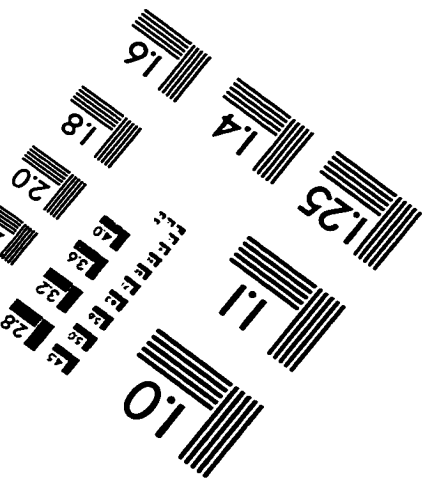
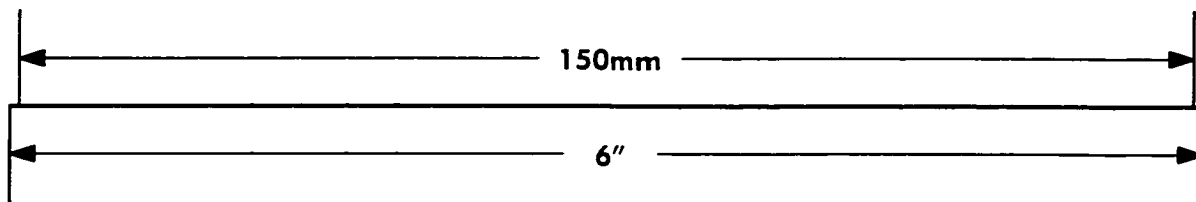
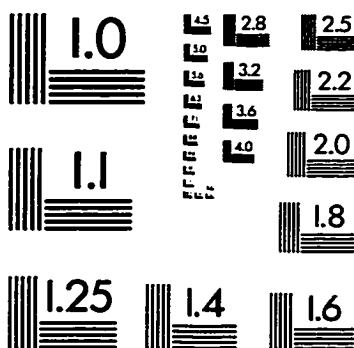
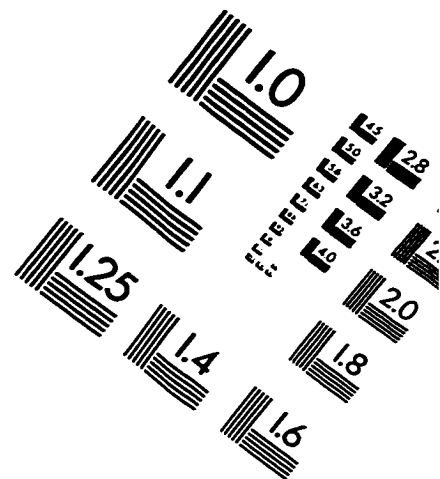
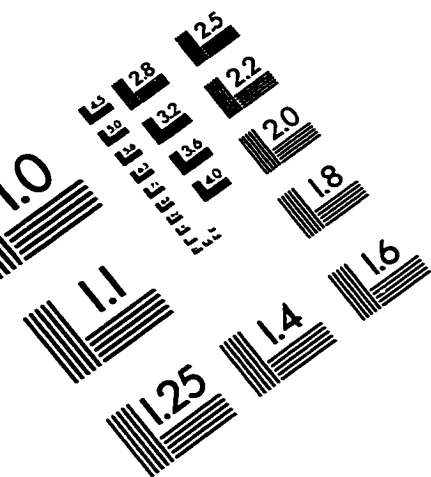
- Bland, M. Brown, D.P. Saunders, P.A. Seidl, C. Fred Moore, K. Maeda, G.S. Blanpied, B.A. Brown, *Phys. Rev.* **C35**, 1388 (1987).
- [Mot95] T. Motobayashi, Y. Ikeda, Y. Ando, K. Ieki, M. Inoue, N. Iwasa, T. Kikuchi, M. Kurokawa, S. Moriya, S. Ogawa, H. Murakami, S. Shimoura, Y. Yanagisawa, T. Nakamura, Y. Watanabe, M. Ishihara, T. Teranishi, H. Okuno, R.F. Casten, *Phys. Lett.* **B346**, 9 (1995).
- [Mue93] A.C. Mueller, B.M. Sherrill, *Ann. Rev. Nucl. Part. Sci.*, **43**, 529 (1993).
- [Nat56] O. Nathan, M.A. Waggoner, *Nucl. Phys.* **2**, 548 (1956).
- [Nor49] L.W. Nordheim, *Phys. Rev.* **75**, 1894 (1949).
- [Ols89] N. Olsson, B. Trostell, E. Ramström, *Nucl. Phys.* **A496**, 505 (1989).
- [Ols90] N. Olsson, E. Ramström, B. Trostell, *Nucl. Phys.* **A513**, 205 (1990).
- [Ost79] F. Osterfeld, J. Wambach, H. Lenske, J. Speth, *Nucl. Phys.* **A318**, 45 (1979).
- [Pet93] R.J. Peterson, *Phys. Rev.* **C48**, 1128 (1993).
- [Rai50] J. Rainwater, *Phys. Rev.* **79**, 432 (1950).
- [Ram87] S. Raman, C.H. Malarkey, W.T. Milner, C.W. Nestor, Jr., P.H. Stelson, *Atomic Data and Nuclear Data Tables* **36**, 1 (1987).
- [Sat83] G.R. Satchler, *Direct Nuclear Reactions*, Oxford University Press, New York (1983).
- [Sch55] G. Scharff-Goldhaber, J. Weneser, *Phys. Rev.* **98**, 212 (1948).

- [Sch96] H. Scheit, T. Glasmacher, B.A. Brown, J.A. Brown, P.D. Cottle, P.G. Hansen, R. Harkewicz, M. Hellstrom, R.W. Ibbotson, J.K. Jewell, K.W. Kemper, D.J. Morrissey, M. Steiner, P. Thirolf, M. Thoennessen, *Phys. Rev. Lett.* **77**, 3967 (1996).
- [She91] B.M. Sherrill, D.J. Morrissey, J.A. Nolen Jr., N. Orr, J.A. Winger, *Nucl. Inst. Meth.* **B56/57**, 1106 (1991).
- [Ste50] H. Steinwendel, J.H.D. Jensen, *Z. Naturforsch.* **5a**, 413 (1950).
- [Ste54] F. Stephens, Jr., F. Asaro, I. Perlman, *Phys. Rev.* **96**, 1568 (1954).
- [Swa94] D. Swan, J. Yurkon, D.J. Morrissey, *Nucl. Inst. Meth.* **A348**, 314 (1994).
- [Til95] D.R. Tilley, H.R. Weller, C.M. Cheves, R.M. Chasteler, *Nucl. Phys.* **A595**, 1 (1995).
- [Tow49] C.H. Townes, H.M. Foley, W. Low, *Phys. Rev.* **76**, 1415 (1949).
- [Win92] J.A. Winger, B.M. Sherrill, D.J. Morrissey, *Nucl. Instr. Meth.* **B70**, 380 (1992).
- [Zuc68] A.P. Zucker, B. Buck, J.B. McGrory, *Phys. Rev.* **C21**, 39 (1968).
- [Zwi83] B. Zwięgliński, G.M. Crawley, J.A. Nolen, Jr., R.M. Ronningen, *Phys. Rev.* **C28**, 542 (1983).

BIOGRAPHICAL SKETCH

The author was born on November 1, 1970 in Annapolis, Maryland. He graduated with high honors from Guilford College in 1992 with a B.S. in Physics and minors in Mathematics and Philosophy. He traveled to Wuppertal, Germany on a Fulbright scholarship to study physics for one year at the *Bergische Universität Gesamthochschule Wuppertal*. The author began his graduate studies at the Florida State University in Fall 1993, receiving a M.S. in Physics in Spring 1994. He fulfilled the requirements for a Ph.D. in Physics in Summer 1997 and will begin work immediately as an Assistant Professor of Physics at Earlham College in Richmond, Indiana.

IMAGE EVALUATION TEST TARGET (QA-3)



APPLIED IMAGE, Inc
1653 East Main Street
Rochester, NY 14609 USA
Phone: 716/482-0300
Fax: 716/288-5989

© 1993, Applied Image, Inc., All Rights Reserved